Check for updates

JGR Solid Earth

RESEARCH ARTICLE
10.1029/2021JB023451

3D GNSS Velocity Field Sheds Light on the Deformation Mechanisms in Europe: Effects of the Vertical Crustal Motion on the Distribution of Seismicity

Jesús Piña-Valdés[1,2], Anne Socquet[2], Céline Beauval[2], Marie-Pierre Doin[2], Nicola D'Agostino[3], and Zheng-Kang Shen[4]

[1]Now at Departamento de Ciencias Geodésicas y Geomática, Escuela de Ciencias y Tecnología, Universidad de Concepción Campus, Los Ángeles, Chile, [2]Université Grenoble Alpes, Université Savoie Mont Blanc, CNRS, IRD, Université Gustave-Eiffel, ISTerre, Grenoble, France, [3]Centro Nazionale Terremoti, Istituto Nazionale di Geofisica e Vulcanologia, Rome, Italy, [4]Department of Earth, Planetary, and Space Sciences, University of California, Los Angeles, CA, USA

Key Points:

- We construct a 3D secular continental-scale Global Navigation Satellite System velocity field over Europe
- A continental-wide surface deformation field provides a means of estimating deformation associated with bulk elastic deformation versus crustal flexure
- The spatial distribution of the seismicity correlates regionally with Strain-rate and vertical velocity patterns, associated to tectonic deformation and crustal flexure respectively

Supporting Information:

Supporting Information may be found in the online version of this article.

Correspondence to:

J. Piña-Valdés,
jesuspina@udec.cl

Citation:

Piña-Valdés, J., Socquet, A., Beauval, C., Doin, M.-P., D'Agostino, N., & Shen, Z.-K. (2022). 3D GNSS velocity field sheds light on the deformation mechanisms in Europe: Effects of the vertical crustal motion on the distribution of seismicity. *Journal of Geophysical Research: Solid Earth*, *127*, e2021JB023451. https://doi.org/10.1029/2021JB023451

Received 18 OCT 2021
Accepted 6 MAY 2022

Author Contributions:

Conceptualization: Jesús Piña-Valdés, Anne Socquet, Céline Beauval
Formal analysis: Jesús Piña-Valdés, Anne Socquet, Marie-Pierre Doin, Nicola D'Agostino
Investigation: Jesús Piña-Valdés, Anne Socquet

© 2022. The Authors.
This is an open access article under the terms of the Creative Commons Attribution-NonCommercial-NoDerivs License, which permits use and distribution in any medium, provided the original work is properly cited, the use is non-commercial and no modifications or adaptations are made.

Abstract Crustal deformation and seismicity in Europe are still poorly understood. Seismic activity is classically ascribed to crustal strain rates generated by edge-driven tectonic forces. However, crustal deformation is not only due to tectonic loading, but can also be related to isostatic and mantellic processes that induce additional stress and strain on the crust by flexure. The influence that those processes have on seismic activity, as well their interaction, is still controversial. The main limitation to study it is because the deformation and its causal mechanisms are usually analyzed separately in small regions. We present here a 3D secular velocity field that covers Eurasia and its plate boundaries including 4,863 Global Navigation Satellite System stations obtained by combining 10 different datasets. We have developed a method based on spatial filtering to identify outliers and smooth the velocity field, and have computed both strain and uplift rate maps that are interpreted in the light of the different driving processes that contribute to the 3D deformation in Europe. The vertical and horizontal deformation features are compared with seismic rates obtained from the spatial and temporal distribution of the seismicity in Europe. Our results suggest that is not possible to explain the seismicity in Europe with edge-driven horizontal tectonic forces only. In some areas markers of the crustal flexure such as the vertical velocity field and its derivative, resulting from buoyancy-driven processes, may help to interpret earthquake distribution.

Plain Language Summary Earthquakes are often related to the deformation of Earth's crust. This deformation is mostly concentrated at the plates boundaries, where most of the earthquakes take place and where the horizontal component of tectonic deformation is stronger. This suggests that the spatial distribution of earthquakes and their frequencies are related to the horizontal deformation rates. However, there is large record of intracontinental earthquakes taking place in regions that do not present significant horizontal deformation, but where vertical deformation is important. This may indicate that vertical deformation, which is usually associated to the downwelling or upwelling of the mantle, can also affect the seismicity. In order to better understand how the crustal deformation processes are related to the earthquake distribution, we combine present-day displacement measurements made in several regions of Europe to develop a 3D deformation model of the ground surface at continental scale, and we compare that model to the distribution and the occurrence rates of earthquakes.

1. Introduction

Crustal deformation in the Eurasian plate and its plate boundaries is the result of a variety of geological processes. These processes have two main origins: first, the far field tectonic convergence between the African plate and Stable Europe plus its local tectonic complexities associated with back-arc extension (e.g., Tyrrhenian, Aegean) or microplate motion (e.g., Anatolia, Adria) (de Vicente & Vegas, 2009; Rosenbaum et al., 2002), and second, buoyancy forces resulting from post-glacial or erosional isostatic rebound, slab detachment, dynamic topography, horizontal gradients of gravitational potential energy etc. (Brandes et al., 2019; Lukk et al., 2019; Nocquet et al., 2016; Sternai et al., 2019). They all contribute to the generation of seismicity in Europe (i.e., Keiding et al., 2015; Mörner, 1991; Mouslopoulou et al., 2016; Walpersdorf et al., 2018). Each of these different geodynamic processes generates characteristic deformation patterns that are superimposed. Thus, while most of the

Methodology: Jesús Piña-Valdés, Anne Socquet
Software: Zheng-Kang Shen
Writing – original draft: Jesús Piña-Valdés
Writing – review & editing: Anne Socquet

continent is characterized by slow, sub-millimetric intracontinental deformation, some areas are distinguished by high rates of horizontal deformation generally in response to tectonic stresses (edge-driven) (Nocquet & Calais, 2004), or other areas, such as in Fennoscandia or the Alps, are dominated by vertical deformation with relatively low horizontal components that are mainly due to isostatic processes (Keiding et al., 2015; Nocquet et al., 2016) or to mantle uplift (Faccenna et al., 2014; Kreemer, 2020).

Over the past decades, the deployment of dense continuous Global Navigation Satellite System (GNSS) observation networks across Europe has increased the density and accuracy of measurements, enabling homogeneous study of deformation processes over the large scale. Historically, those studies were concentrated on tectonically active regions and, to a lesser extent, on regions that undergo important isostatic re-equilibration processes. As a result, in most studies, the deformation styles and magnitude within slowly deforming areas are not well characterized, or they are imaged piecewise (country by country), failing to provide the understanding that would be brought by a large-scale picture. This was acknowledged by some pioneering studies that initiated the efforts to provide large scale velocity and deformation fields (e.g., Devoti et al., 2017; Faccenna et al., 2014; Kenyeres et al., 2019; Kreemer, 2020; Nocquet, 2012; Nocquet & Calais, 2003; Nocquet et al., 2001; Serpelloni et al., 2013).

Still, to date, a high-resolution integrated 3D secular velocity field and its associated strain rate field in Europe and its boundaries is missing. The generation of such velocity field requires solving two issues: (a) generate a procedure to combine GNSS velocities derived from different GNSS data observation quality and processing methods, able to deal with the different uncertainty estimates; and (b) handle the uncertainty level of the GNSS measurements in slowly deforming areas, which are of the order of the intracontinental deformation. These problems make it complicated to estimate the strain rates in slowly deforming regions, as the GNSS velocity noise may hide the deforming processes at stake and prevent from properly estimating the tectonic strain rates.

In the present work we combine, at the velocity level, ten GNSS velocity fields with different spatial coverages and derive a high-resolution 3D velocity field for Europe, spanning both tectonically active regions and slow-deforming zones. The velocity estimates are validated based on their spatial consistency and their level of uncertainty, allowing for an identification of outliers. The deformation styles and associated strain rates values are then computed over the whole European continent, at a high spatial resolution. Using these informations on horizontal strain rates, deformation style and vertical velocity field we characterize the spatial variation of the main forces (edge-driven vs. buoyancy-driven or mantle-driven), and evaluate their impact on the spatial distribution of seismicity.

2. GNSS Velocity Field Combination

In order to obtain a velocity field of excellent quality level, the best way to proceed would be to gather for all GNSS stations in Europe, the Receiver INdependent EXchange RInEx data and fully-documented associated metadata, in order to process them together in a self-consistent geodetic solution. The EUREF permanent network (EPN, http://www.epncb.oma.be, a federation of agencies, research institutions and universities) operates geodetic class GNSS stations at the scale of the European continent, and delivers fundamental geodetic products, such as RInEx data and position time series, used to build the global International Terrestrial Reference Frame (ITRF). To complement this effort, the European Plate Observing System (EPOS, http://www.epos-eu.org) aims at facilitating the use of integrated data and products in the field of geosciences. For the geodesy part, EPOS works hand-in-hand with the EPN, and completes the data coverage by including progressively national and regional GNSS networks in their data and product portals (https://gnss-epos.eu/). However, in spite of these efforts, the data of several GNSS stations are currently not readily available to the scientific community. Several networks owned by private companies, local administrations or even national networks do not (yet) distribute their data and metadata publicly.

When RInEx data are not available, various position or velocity solutions can be combined together to obtain a velocity field that is wider or denser than each individual input solution. The combination procedure homogenizes the different input solutions and mitigates systematic errors. Stations common to several solutions allow to tie these into a single and consistent reference solution and provide information on the relative systematic biases between each individual solution, including potential alignment errors with respect to the reference frame (Kenyeres et al., 2019; Legrand & Bruyninx, 2009; Legrand et al., 2012).

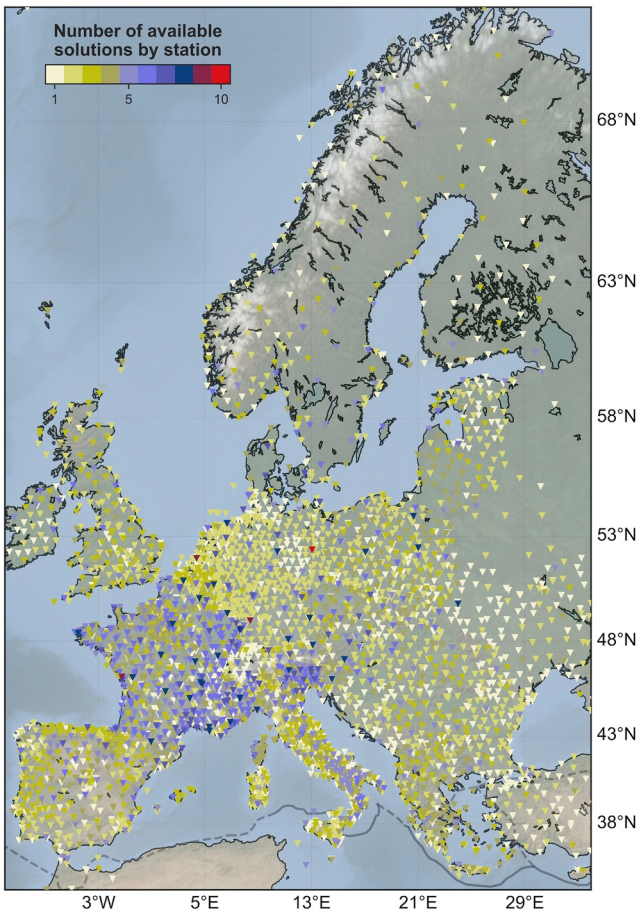

Figure 1. Spatial distribution of the Global Navigation Satellite System stations considered in this study, color-coded by the number of independent velocity estimations at each station.

An approach classically used in geodesy, is to perform a geodetic combination of independent daily (or weekly) GNSS solutions, often distributed in Solution INdependent EXchange (SInEx) format that provides the full variance covariance matrix of the solution:

1. A first step, consists in computing a daily (or weekly) position solution to combine individual position files from all contributions, thus generating a series of combined daily (or weekly) position SINEX files.
2. In a second step, these pre-combined files then enter into a multi-year combination to produce a cumulative position and velocity solution. Such an approach is routinely applied on the global level within the International GNSS Service (IGS) or for the realization of the ITRF (Altamimi et al., 2016). On the regional level, such approach is performed in South America for the SIRGAS network (Sánchez et al., 2016), in Europe for the EPN (Bruyninx et al., 2012) and the EPN Densification project (Kenyeres et al., 2019), and in north America, for the Plate Boundary Observatory (Herring et al., 2016).
3. Finally, the GNSS muti-year solution is tied to a realization of the ITRF, using a set of reference stations, and following the Minimum Constraint approach (Altamimi et al., 2002), in order to avoid any distortion of the position and velocity estimates. In other words, constraints are applied only on the geometric transformation parameters and not directly on stations positions or velocities (Sillard & Boucher, 2001).

Finally, the simplest and easiest option is to combine the different solutions at the velocity level (e.g., Devoti et al., 2017; Kreemer et al., 2014). The velocity combination procedure is a generalization of the loosely constraints approach (Davies & Blewitt, 2000), for which the knowledge of the position estimates is not needed. Although subject to some shortcomings, this approach allows to efficiently obtain a combined velocity solution, including when daily or weekly solutions are not available, or when the full variance-covariance matrix is not available for the multiyear solutions. In the following, we present the details of the combination procedure performed in this paper. The possible biases and the overall quality is checked and estimated at common stations. Outliers are then detected using the spatial consistency of the obtained velocity field. Because we do not have all the variance– covariance matrix, we propose a simple harmonization of the uncertainties. Even though we may experience some biases caused by different processing standards used to compute the different solutions, and lose information on the quality of each individual velocity because of the lack of direct access to position time series, our approach allows to obtain a combined solution that is the most dense and wide to date, and gives interesting insights on the deformation of Europe.

2.1. Selected GNSS Velocity Solutions

To generate a combined velocity field solution that covers the entire Europe, we look for previously published velocity solutions, with the requirement that the different databases complement each other. Finally, ten velocity fields are included in the present analysis (Figure 1):

1. **EPOS-UGA solution in double difference:** This GPS velocity solution (doi:https://doi.org/10.17178/GNSS.products.Europe) was processed in double difference, using GAMIT software (Herring et al., 2018). Velocities have then been estimated through a statistical analysis of the position time-series using MIDAS Software (Blewitt et al., 2016). The velocity field is given with respect to the stable Eurasian plate as defined from ITRF2014 (Altamimi et al., 2016). The solution provides the vertical and horizontal velocities with their respective uncertainties for 1092 GPS stations, most of them located in metropolitan France and Italy, as well as some more sparse information in United Kingdom, Scandinavia, Germany, Greece and the Iberic peninsula.

2. **INGV Solution (INGV**; D'Agostino N., 2019, personal communication**):** This GPS velocity solution was processed in Precise Point Positioning (PPP) (Zumberge et al., 1997) using GIPSY (Webb, 1997), and followed by a common mode estimation. Velocities have been estimated through a statistical analysis of the position time-series using MIDAS Software (Blewitt et al., 2016). The velocity field is given with respect to the stable Eurasian plate as defined from ITRF2014 (Altamimi et al., 2016). This solution contains the vertical and horizontal velocities with their respective uncertainties for 662 GPS stations. Most stations are distributed in the French and Italian Alps. This data set also contains information in metropolitan France, in the Northern Iberic peninsula, as well as more sparse information in the United Kingdom and Germany.
3. **NGL Solution for Europe (NGL):** This GPS velocity solution (Blewitt et al., 2018) was processed automatically in PPP, using GIPSY (Webb, 1997). Velocities have been estimated through a statistical analysis of the position time-series using MIDAS Software (Blewitt et al., 2016). The velocity field is given in the IGS14 reference Frame (Altamimi et al., 2016). This solution provides the vertical and horizontal velocities with their respective uncertainties for 4095 GPS stations in Europe. This data set shows a high density of stations in France, United Kingdom, Italy, Iberic peninsula, Greece as well as more sparse information in the rest of Europe.
4. **Switzerland Solution (ETH):** This GPS velocity solution (Sánchez et al., 2018a, 2018b) was processed in double-difference with Bernese (Dach et al., 2015). The velocities have been estimated using multi-year solutions. The velocity field is given in IGb08 reference frame (Rebischung, 2012). This solution provides the vertical and horizontal velocities with their respective uncertainties for 287 GPS stations. Most of the stations are located in Switzerland, a few of them are in France and Italy.
5. **France Solution (MONT):** This GPS velocity solution (Masson et al., 2019a, 2019b) was processed in PPP, using a software developed by the Canadian Geodetic Survey of Natural Resources Canada (CSRS-PPP v1.05) (Héroux & Kouba, 2001). Velocities were derived from daily position time series analysis, through a trajectory model. Velocity errors were computed using Williams (2003)'s generic expression for colored noise with a non-integer spectral index. The velocity field is given with respect to the stable Eurasian plate as defined from ITRF2014 (Altamimi et al., 2016). This solution provides the vertical and horizontal velocities with their respective uncertainties for 934 GPS stations, with a high density of stations in France, Switzerland, and a lower density in Italy and Spain.
6. **Scandinavia Solution (KIER):** This GPS velocity solution (Kierulf et al., 2021) was processed in double difference, using GAMIT software (Herring et al., 2018). Velocities were estimated using a multiyear geodetic combination and velocity uncertainties are based on time series analysis using Cheetah (Bos et al., 2008), including a combination of white noise and power-law noise. The velocity field is given as defined from ITRF2008 (Altamimi et al., 2011). This solution provides the vertical and horizontal velocities with their respective uncertainties for 164 GPS stations in Scandinavia.
7. **Central Europe Solution (CEUR):** This GPS velocity solution (Zurutuza et al., 2019) is derived from weekly solutions of 10 subnetworks processed with Bernese (Dach et al., 2015). The velocity field is obtained from the combination of individual sub-network velocities through a 7-parameter Helmert transformation (Watson, 2006). The velocity field is given with respect to the stable Eurasia plate as defined from ETRF2000. This solution provides the vertical and horizontal velocities with their respective uncertainties for 1269 GPS stations mainly located in Poland, Czech Republic, Slovakia, Slovenia, Croatia, Hungary and Serbia.
8. **NW Europe solution (KREE):** This GPS velocity solution (Kreemer, 2020; Kreemer et al., 2020) was processed in PPP, using GipsyX software (Bertiger et al., 2020). Velocities and their uncertainties were derived from filtered daily position time series, using MIDAS Software (Blewitt et al., 2016) and spatially varying robust estimation of the common modes (Kreemer & Blewitt, 2021). The velocity field is given in IGS14 reference frame which is compatible with ITRF2014 (Altamimi et al., 2016). The solution provides vertical and horizontal velocities and their uncertainties for 2383 GPS stations, located in North-West Europe between latitudes 38°N and 64°N.
9. **Balkans solutions (BALK):** This horizontal GPS velocity solution (D'Agostino et al., 2020) was processed in PPP (Zumberge et al., 1997) using GIPSY (Webb, 1997), followed by a common mode estimation. Velocities have been estimated through a statistical analysis of the position time-series using MIDAS Software (Blewitt et al., 2016). The velocity field is given with respect to the stable Eurasian plate as defined from IGS14 (Altamimi et al., 2016).

10. **Dense solution of the EUREF Permanent Network (EPND):** This multiyear GPS velocity solution (Kenyeres et al., 2019) was obtained by combining weekly solutions of 27 analysis centers with CATREF software (Altamimi et al., 2007). The velocity field is given in the ITRF2014 (Altamimi et al., 2016). This solution provides the vertical and horizontal velocities with their respective uncertainties for 2264 GPS stations in Europe.

2.2. Transformation Into a Common Reference Frame

The solutions considered do not refer to the same reference frames, or the reference frame realization may slightly differ from one solution to the other. To compare and combine them, it is necessary to project all velocity fields into a common reference frame.

We use EPND solution (Kenyeres et al., 2019) as reference because it is based on the EPN multiyear solution (e.g., Legrand & Bruyninx, 2009; Legrand et al., 2012), that is a local densification of the ITRF2014 (Altamimi et al., 2016). In addition this solution includes a large number of stations both in western and eastern Europe, therefore offering a good coverage and a large number of tying point for all other solutions.

We align all other solutions to EPND solution in ITRF2014 by applying a 6-parameter Helmert Transformation using the velrot module of GAMIT/GLOBK package (Herring et al., 2018), considering 3 parameters of translation, 3 parameters of rotation, and no scaling factor in order to avoid potential changes in the internal deformation (Watson, 2006). The 6 parameters of the Helmert transform are inverted using a least square algorithm that minimizes the difference of the three components of the velocities at common stations between EPND solution and each individual solution. The values of the transformation parameters for the different velocity solutions are summarized in Table S1 in Supporting Information S1.

Then the aligned velocity solutions are rotated with respect to the stable Eurasian plate as defined from ITRF2014 by applying the pole (55.07°N, 99.09°W, 0.261°/Myr) (Altamimi et al., 2016). A synthetic view of the different solutions used, once rotated in ITRF2014 realization of the stable Eurasian plate (Altamimi et al., 2017), is provided in Figure 2.

2.2.1. Comparison of Solutions

Once projected into a common ITRF2014 reference frame, the similarity of the different solutions is explored by comparing the horizontal and vertical velocities at common stations (Figure 3 and Figure 4), and the horizontal azimuths (Figure 4—top right panel). The velocity residuals at common stations mostly show a normal distribution centered on zero. Their dispersion represents the variability from one solution to the other, which typical standar deviation is less than 1 mm/year. Dispersions on the vertical velocity differences are larger than the horizontal ones, that reflects the larger uncertainty associated with vertical velocity estimates. Similarly, the distribution of azimuth residuals indicates that most stations have similar horizontal velocity direction. Hence there is no systematic difference between the solutions at common stations once they are projected in the same reference frame. The largest dispersions are observed on datasets that have a limited number of common stations, or on datasets mostly centered on regions with large velocities (i.e., tectonically active areas) or uncertainties, such as CEUR or BALK datasets that host a large number of stations in Italy or in the Balkans. The standard deviation of the CEUR solution, is larger than the one of other solutions, maybe reflecting a larger uncertainty in the velocities associated with this solution.

Also, for each transformed solution, the residual with respect to ITRF2014 velocities at each IGS station is also computed and summarized in Figure S1 in Supporting Information S1. The results of this comparison suggest that the projection of the solutions in a unique reference frame is coherent, since they show an agreement at the 0.5 mm/year on the horizontal components for 83% of the common stations compared. The sites that show strong differences are the same in most of the solutions, rather reflecting a variability on those sites velocity estimates than a reference issue.

2.3. Relative Weighting of the Solutions

Our objective while combining the different solutions is to provide a single velocity solution per station, considering all the information available and taking into account a relative weighting based on the intrinsic quality of

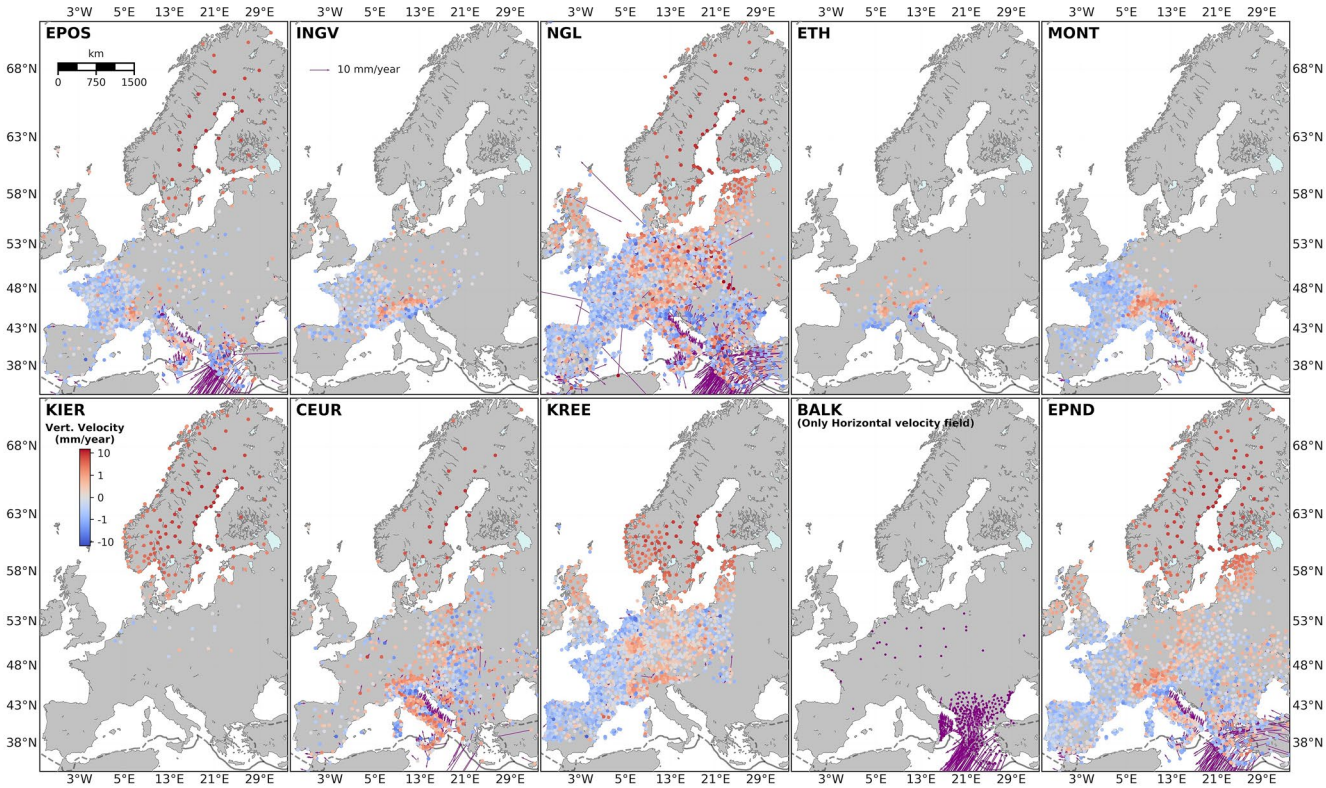

Figure 2. Velocity field solutions rotated into the stable Eurasian plate realization of the ITRF2014 reference frame (Altamimi et al., 2016; Altamimi et al., 2017). Circles represent the position of the GPS stations color-coded by the amplitude of vertical velocities. Arrows represent the direction and the amplitude of the horizontal velocities. Upper row from left to right– European Plate Observing System-UGA solution (Deprez et al., 2019), INGV solution, NGL solution (Blewitt et al., 2018), ETH solution (Sánchez et al., 2018a), MONT solution (Masson et al., 2019b), Bottom row from left to right—KIER solution (Kierulf et al., 2021), CEUR solution (Zurutuza et al., 2019), KREE solution (Kreemer, 2020), BALK solution (D'Agostino et al., 2020), EPND solution (Kenyeres et al., 2019).

each data set. This implies to solve the following issues: (a) deal with the different levels of uncertainties of the solutions, that depend on the processing method and the manner uncertainties are estimated, and (b) filter out or downweight the outlier values, or those associated with high uncertainties.

2.3.1. Uncertainty Harmonization

The accuracy and precision of GPS velocity field solutions depends on the technical characteristics of the GNSS stations (antenna, receiver, monument, site effects), on the quality of the metadata, on the amount of data processed, on the time span of the data, on the quality of the GNSS data processing (automated processing, manual processing, double difference, PPP, etc.), and on the method used to estimate the velocity (formal geodetic combination, trajectory model of the time series, statistical analysis of the time series, etc.). Even for the same GNSS data inputs, the processing method chosen by different authors will impact the velocity field solution and its estimated uncertainty. For example, it is well known that uncertainties derived from formal geodetic solutions can be underestimated if a proper noise level is not used when estimating the secular velocity. On the other hand, time series analysis usually provides larger uncertainties associated with the velocities, since time-correlated noise affects the velocity estimate. Finally, statistical analysis of the position time series (with MIDAS software for example (Blewitt et al., 2016)) usually leads to even larger uncertainties associated with the velocities, that are computed from the standard error of the distribution histogram. This situation complicates the combination of different velocity field solutions, associated with multiple values for common stations that are not fully compatible between each other.

To overcome this problem, a procedure must be established for harmonizing the uncertainties.

The uncertainties of the velocities, for the ten data sets used in this work, follow a log-normal distribution (Figure S2 in Supporting Information S1). Their amplitudes and dispersions can strongly differ from one solution to the

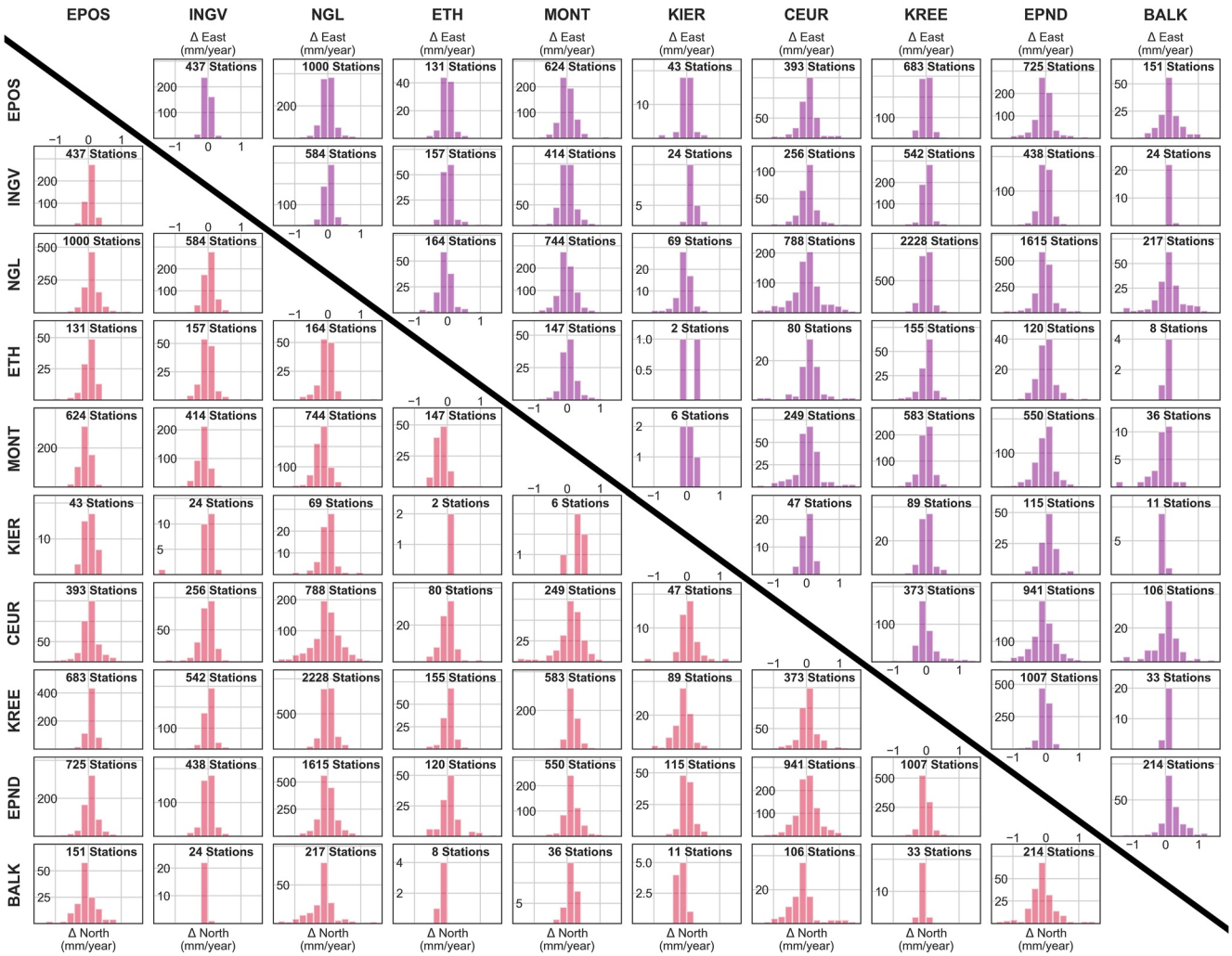

Figure 3. Histograms of horizontal velocity differences at common stations, by pairs of velocity field solutions. Upper triangle—differences in East component. Lower triangle—differences in North component. The number of common stations between each data set is indicated in the upper part of the histograms.

other. For the uncertainties to be comparable, we rescale the uncertainties of ETH, KIER, MONT, CEUR, KREE and EPND solutions to a level compatible with uncertainties coming out of MIDAS (EPOS-UGA, INGV, NGL, BALK).

The uncertainty scaling has been done through modeling the log-normal distributions, independently for the three components on each solution. The logarithm of the uncertainties follows a normal distribution. Each normal distribution is characterized by its mean ($\ln(\mu)$) and standard deviation (σ). Then, the percentile "P_x" corresponding to the velocity uncertainty "δ" can be obtained using the Cumulative Distribution Function (CDF) defined as:

$$P_x(\delta) = \Phi\left(\frac{ln(x) - ln(\mu)}{\sigma}\right)$$

where Φ is the CDF of the normal distribution with zero mean and $\sigma = 1$ unit standard deviation.

The scaled uncertainty "x_s" has the same CDF as the original uncertainty "x", but in a lognormal distribution of reference with central tendency parameters μ_r and σ_r, that can be obtained from the CDF, called Percent Point Function (PPF):

$$\delta_s = e^{\mu_r + \sigma_r \Phi^{-1}(P_x(\delta))}$$

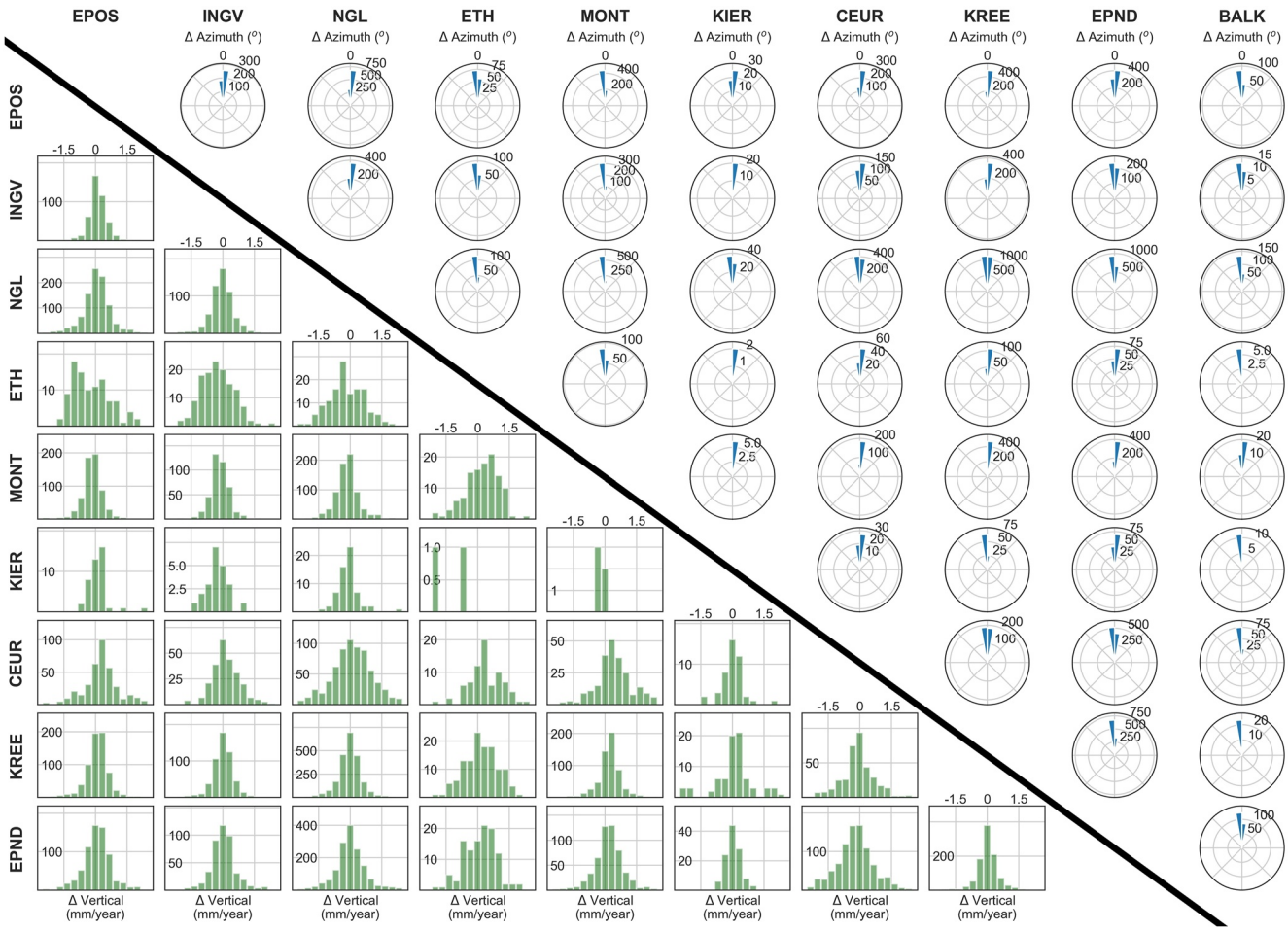

Figure 4. *Upper triangle*—Radial histograms of velocities azimuthal difference at common stations, by pairs of velocity field solutions. Bottom triangle—Histograms of vertical velocity differences at common stations, by pairs of velocity field solutions.

where Φ^{-1} is the PPF of the normal distribution.

For this work, the velocity uncertainties distribution of the EPOS-UGA solution has been chosen as reference for the log-normal distribution. The uncertainties of the Vertical, East and North velocities of the ETH, KIER, MONT, CEUR, KREE and EPND solutions were scaled in order to fit the reference log-normal distribution (Figure S3 in Supporting Information S1).

2.3.2. Removal of Stations With Largest Uncertainty

The stations that exhibit the largest uncertainties have been removed from each data set. Given that the East and North uncertainty components display similar distributions for most solutions (Figure S2 in Supporting Information S1), East and North uncertainties were merged into a unique horizontal uncertainty:

$$\delta_{hor} = \sqrt{\delta_{East}^2 + \delta_{North}^2}$$

For each solution, a new lognormal model was fitted to the distribution of horizontal velocity uncertainties. The stations exhibiting uncertainties larger than the 99th percentile were removed from the datasets. Stations with largest uncertainties on the vertical velocity were removed with a similar procedure.

Table 1
Uncertainty Thresholds Applied for Station Classification Into Groups A, B, and C

	A		B		C	
Class	Active	Stable	Active	Stable	Active	Stable
Horizontal Uncertainty (mm/y)	<0.5	<0.25	0.5–0.75	0.25–0.375	0.75–1	0.375–0.5
Vertical Uncertainty (mm/y)	<1.5	<0.75	1.5–2	0.75–1	2–3	1–1.5
Number of Stations	3377		714		377	

Note. Lower thresholds are defined for stable plate interiors than for active tectonic regions.

2.3.3. Weighted Average of Velocities at Each Measurement Point

After removing the stations with the largest velocity uncertainties and harmonizing the uncertainties of the solutions, we combine all the information into a single velocity solution. At stations for which more than one velocity solution is available, we compute a weighted average velocity using the uncertainty of the velocity solutions:

$$\dot{V}_k = \frac{\sum_{i=1}^{n} \frac{V_{ki}}{\delta_{ki}}}{\sum_{i=1}^{n} \frac{1}{\delta_{ki}}}$$

where $\dot{V}_k$ is the weighted average velocity of the station in the k velocity component (North, East or vertical direction), n is the number of solutions that provide a velocity for the station, V_{ki} corresponds to the velocity of the station on the component k in the solution i, and δ_{ki} is the uncertainty of the velocity for the component k in the solution i.

The weighted average velocity uncertainty is computed as follow:

$$\dot{\delta}_k = \frac{n}{\sum_{i=1}^{n} \frac{1}{\delta_{ki}}}$$

3. Filtering of the Combined Velocity Field

The combined velocity field (Figure S4 in Supporting Information S1) shows locally some anomalous velocity values or high uncertainties that are inherited from the original solutions (see Figure 2 for comparison with the original velocity fields). Since the strain rate estimation is sensitive to the scatter, additional filters will be applied to the combined solution before the strain rate computation.

We test here the effect of three different cascading filters: (a) stations removal based on the velocity uncertainty level, (b) identification and removal of outliers based on the spatial consistency of the velocities and (c) spatial smoothing of the velocities.

3.1. Removal of Stations by Velocity Uncertainty Level

This is a simple and direct way to eliminate poorly constrained values of the velocity field, as reflected in their uncertainties. A noise level threshold is proposed to classify the quality of the GPS stations into 3 categories: A, B and C (Table 1). Since stations affected by important level of seismic activity are associated with higher uncertainties on their velocity estimate than stations located in plate interiors (characterized by stable time series—Figure S5 in Supporting Information S1), we propose a different threshold value on tectonically active regions and on stable ones (Table 1). The active tectonic regions in Europe are considered to be the regions that are directly affected by the collision with the African plate: the Hellenic subduction, the Apennines, the south of Italy (Sicilia) and the south of the Iberic peninsula.

Selecting only high-quality stations falling in class A (very conservative criterion) would reduce dramatically the number of stations (from 4,863 stations in total, to 3377) in the combined velocity field.

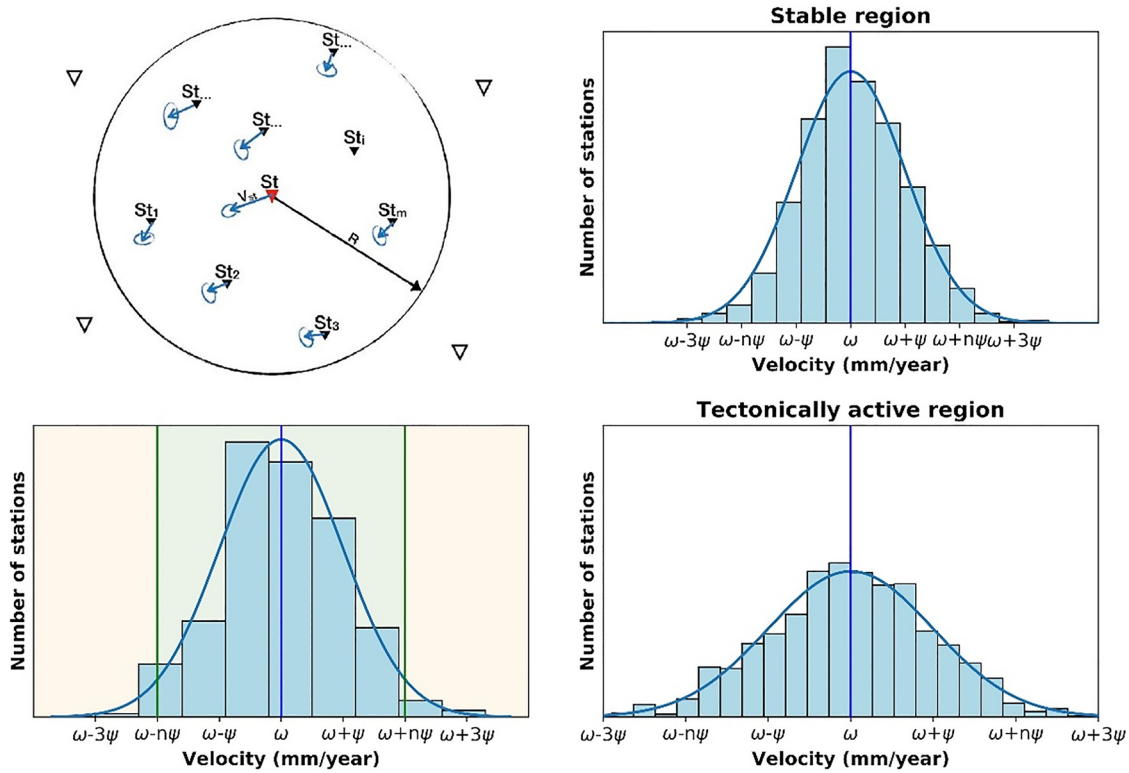

Figure 5. *Upper Left*—Sketch region of radius R around a GPS station ("St" in red), inside which velocities are assumed spatially coherent. Blue arrows and ellipses represent the Global Navigation Satellite System (GNSS) velocities and uncertainties. "di" represent the distance between the station "St" and station "Sti." *Bottom Left*—Sketch of the velocity distribution of the GNSS stations inside the region; "ω" and "ψ" are the mean and standard deviation of the velocity distribution; Green vertical lines indicate the tails of the distribution. If station "St" falls in the tails it is either classified as outlier (see Section 3.2) or identified to be smoothed (see Section 3.3). *Upper Right*—Example of velocity distribution in a stable region. *Bottom right*—example of velocity distribution in an active region. Note that the velocity distribution in an active region has a larger standard deviation "ψ" than in a stable region.

3.2. Identification and Removal of Outliers

To identify outliers in the combined velocity field, a criterion that evaluates the agreement between neighboring stations has been used. It is based on the assumption that the velocity field should be coherent within a region surrounding each station, and no velocity should significantly differ from its neighbors. We assume that the distribution of station velocities within a given region can be modeled with a normal distribution. A region defined by a circular area of radius "R" from a given station is considered; the mean of the station velocities in that region is "ω" and its standard deviation is "ψ" (Figure 5). Stations with velocities in the tails of the distribution are considered as outliers, that is, stations with velocities:

$$V_{st} < \omega - \tau * \psi \quad \text{or} \quad V_{st} > \omega + \tau * \psi$$

where "τ" is an integer value chosen to define the threshold. Despite the simplicity of this criterion, it is a powerful tool for outlier identification in a large variety of deformation context. In tectonically stable regions, where low velocity variability is expected, the velocity distribution is expected to be narrow (Figure 5). Station velocities that differ slightly (a few mm/year) from the median will be considered as outliers. On the other hand, in actively deforming areas, the velocity distribution is expected to be more spread out and only velocities that are much larger or much lower than the mean will be considered as outliers.

We must then define the radius "R" of the considered area, and the threshold "τ" that characterizes the tails of the distribution. The choice of the tail threshold is crucial, small tail threshold can generate false detections, while a conservative tail threshold could fail in detecting outliers. Since each component of station velocities is independent, this verification must be done in the three velocity directions. Tests are only performed in regions of radius "R" that contains at least 4 stations besides the evaluated one.

3.3. Velocity Field Smoothing

The last filter tested here is meant to reduce the regional scatter in the combined velocity field to avoid artifacts in the strain rate estimation, which is critical in low deformation regions.

Assuming that the uncertainties on station velocities are spatially uncorrelated, in very dense instrumented regions an improved GNSS velocity field could be extracted by averaging the measurements. This will tend to cancel the random noise, while consistent signals will be conserved.

Similarly to the identification of outliers, it is assumed that the velocity field is coherent in a region surrounding the stations. Again, a circular area of radius "R" from a given station is considered. The uncertainty on the velocity at the station corresponds to "δ_{st}", while "μ_s" and "σ_s" are the mean velocity and the standard deviation of the distribution of velocities for stations within that region (Figure 5). The station velocity is smoothed if:

$$\tau * \delta_{st} \geq \sigma_s$$

where "τ" is the threshold ratio between spatial variability and station uncertainty.

This smoothing criterion favors the smoothing of stations with large velocity uncertainty in environments where velocity is highly coherent. Instead, if the coherence of neighboring stations or the station's velocity uncertainty decreases, the station has less chance to be smoothed. Therefore, in tectonically stable regions characterized by low deformation, where the velocity distribution is expected to be narrow and coherent, the stations have more chances to be smoothed. On the other end, in tectonically active areas, the velocity distribution is expected to be wider and the velocity uncertainties higher, the possibility to activate the smoothing criterion is lower.

This criterion is applied in the three velocity directions. If the region of radius "R" contains at least 5 stations besides the evaluated one, and if the uncertainty of the station falls in the tail of the distribution for at least one of the components, the velocities are smoothed in the three directions as follows:

$$\dot{V}_k = 0.5 \times V_k + 0.5 \times \frac{\sum_{i=1}^{n} \frac{V_{ki}}{d_i}}{\sum_{i=1}^{n} \frac{1}{d_i}}$$

where $\dot{V}_k$ is the weighted smoothed velocity for the k velocity component (North, East or vertical), n is the number of stations inside the region, V_{ki} correspond to the velocity component k of the station i, and d_i is the distance between the station and station i. A similar procedure is applied to smooth the uncertainty of the velocity for each component k:

$$\dot{\delta}_k = 0.5 \times \delta_k + 0.5 \times \frac{\sum_{i=1}^{n} \frac{\delta_{ki}}{d_i}}{\sum_{i=1}^{n} \frac{1}{d_i}}$$

For this criterion, as in Section 3.2, we need to fix the radius "R" of the region around each station where the velocity field is considered coherent. This radius has an impact on the number of stations involved in the smoothing and needs to be explored, as well the threshold value "τ" that controls the sensitivity of the smoothing criteria.

3.4. Sensitivity Analysis for the Filtering Parameters of the Combined Velocity Field

Since the filtering of the velocity field depends on parameters that need to be defined, a sensitivity analysis has been performed in order to observe the impact of those parameters on the number of filtered and smoothed stations of the combined data set:

For the removal of stations with high velocity uncertainty, 4 different cases have been considered:

1. Keep only the stations of Class A.
2. Keep the stations of Class A and B.
3. Keep the stations of Class A, B and C.
4. Consider all the stations.

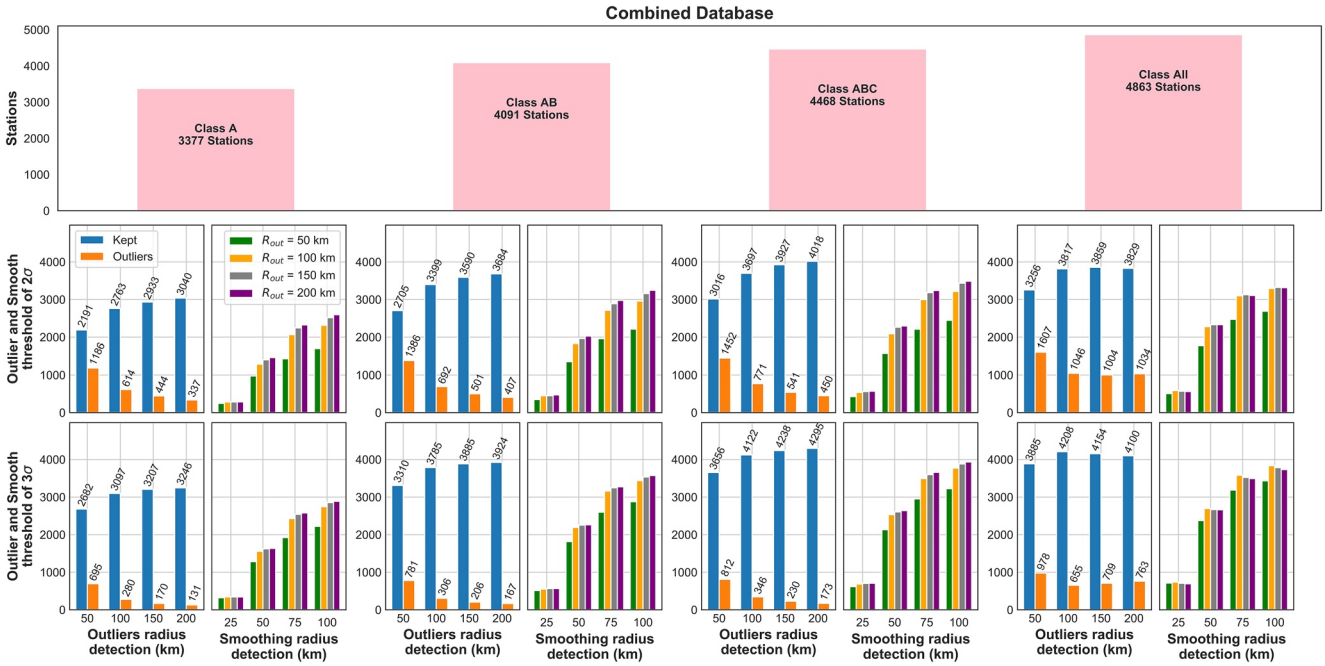

Figure 6. Sensitivity analysis on the parameters used in the procedure to filter the combined velocity field: impact on the number of stations affected at each stage. The figure can be read as a table. The top row shows the number of stations included in the combined solution, depending on their quality class (Table 1). The two bottom rows show the impact of the tail threshold value "τ" (2 or 3) used to identify outliers and or smoothing candidates. In each cell, the left diagram shows the impact of the radius used to define the outliers on the number of stations kept (blue bar) and the number of outliers (orange bar), while the diagram on the right shows the effect of the radius used for the smoothing criterion (colors refer to the different outlier radius used).

For the identification of outliers, 4 different Radius "R" (50, 100, 150, and 200 km) and two threshold values "τ" (2 and 3) have been tested.

For the smoothing of the velocities, 4 different Radius (25, 50, 75 and 100 km), and two threshold values "τ" (2 and 3) have been tested.

Figure 6 summarizes the results of the sensitivity study, and shows for each combination of parameters the number of stations kept in the solution, the number of stations considered as outliers, and the number of stations where the velocity is smoothed. It is possible to see that the smaller the radius considered for outlier identification, the larger is the number of outliers detected. Whereas for the smoothing criterion, the larger the radius of the area considered, the larger is the number of stations smoothed. Finally, it is important to note that using a large threshold value for detecting outliers or for the smoothing implies that less velocities are removed from the database.

To choose the outlier detection and smoothing radius for our preferred solution, we analyze three quantitative metrics in addition to our sensitive study: (a) the total number of stations N_i kept in each filtered solution i, (b) the number of velocities smoothed Nv_i, and (c) the variance reduction between each filtered solution i and the raw solution. The raw solution (all class stations, with no outliers removed and no velocities smoothed) has 4,863 stations. The filtering process diminishes the total number of stations and increases the number of smoothed velocities. However it is noticeable in Figure 6 that these values stabilize and reach a plateau with increased filtering. Our solution is picked as a compromise between the necessary cleaning of the solution and the will to keep as much as possible relevant information and details in the solution. Figure S6 in Supporting Information S1-Top shows for each solution N_i as a function of Nv_i. Our preferred solution is plot with a star, and the median of the values are also indicated. This plot shows that the solution we picked performs a reasonable filtering of the velocities, at least in terms of number of stations filtered. we also look at the variance reduction between each solution i and the raw solution by computing:

$$\mathrm{nRSM}_i = \sum_{j=1}^{j=N_i} \frac{\sqrt{\left(VE_j^i - VE_j^{raw}\right)^2 + \left(VN_j^i - VN_j^{raw}\right)^2}}{N_i}$$

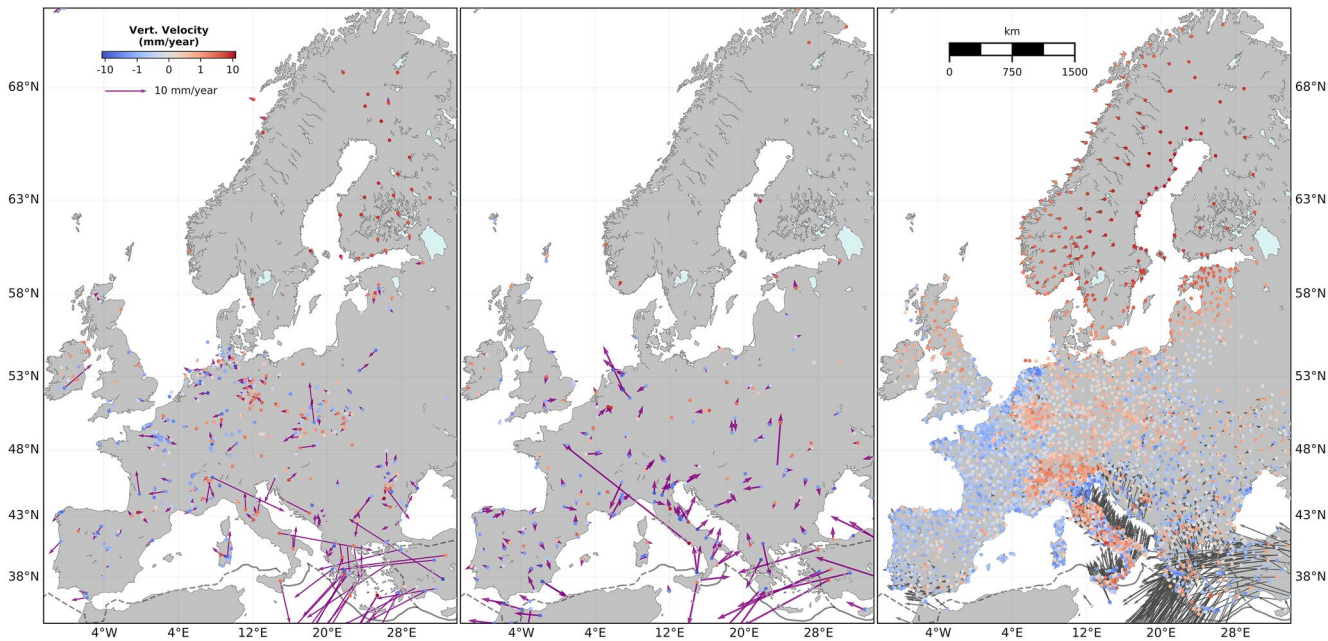

Figure 7. Preferred solution filtering results. From left to right: bad quality stations not included in classes A, B, and C (395 stations); stations identified as outliers (230 stations); remaining stations after filtering bad quality stations and outliers (4,238 stations).

where Ni correspond to the number of of station in each solution i, VE_j^i and VN_j^i correspond to the East and North velocity component of station j in solution j, and VE_j^{raw} and VN_j^{raw} East and North velocity component of station j of combined data set non filtered.

We plot $nRMS_i$ as a function of R_{out} and R_{smooth} for the different solutions tested (Figure S6 in Supporting Information S1 - Bottom). Our preferred solution is indicated with a star. This graph shows that the variance reduction is important with the first outliers detected, and then flattens with the smoothing and outlier detection radius.

The preferred solution is therefore chosen as being the solution that shows a good compromise between number of station kept in the solution and variance reduction, in other word, we keep a solution from which aberrant values have been removed (variance reduction) but that keeps enough density of information (we try to minimize the number of outlier and smoothed velocities). The filtering results of our preferred solution (shown in Figure 7), and the processed combined velocity field (Figure 8), corresponds to the following filtering parameters:

1. Considering A, B and C class stations.
2. Radius of 150 km for the outlier detection.
3. Radius of 50 km for the decision to smooth spatially.
4. Threshold for outlier detection or smoothing of three.

This solution generates a total number of 4468 A, B and C Class stations distributed all over Europe. Out of these 4,468 stations, 346 where identified as outliers and removed. Out of the remaining 4,238 stations, 2,615 were smoothed (61.7% of the remaining stations). This solution seems to be a good trade-off between density of information, level of uncertainty, reliability of the velocities, and spatial variability of the solution. The obtained velocity field exhibits the main features of the deformation that were previously observed in other studies, such as the uplifting of the Alps (i.e., Nocquet et al., 2016; Walpersdorf et al., 2018) and Scandinavia (Keiding et al., 2015) or the tectonic deformation in the Balkans (D'Agostino et al., 2020) and Italy (Métois et al., 2015).

4. 3D Strain Rate Estimation Using Elastic Solid Assumption

Since the preferred combined velocity field solution presents a good coverage of Europe, it can be used to estimate well-constrained strain rates. To do so, the velocities have been interpolated on a discrete grid of 0.01° steps using VISR software (Shen et al., 2015). This software has been modified in order to derive the 3D strain

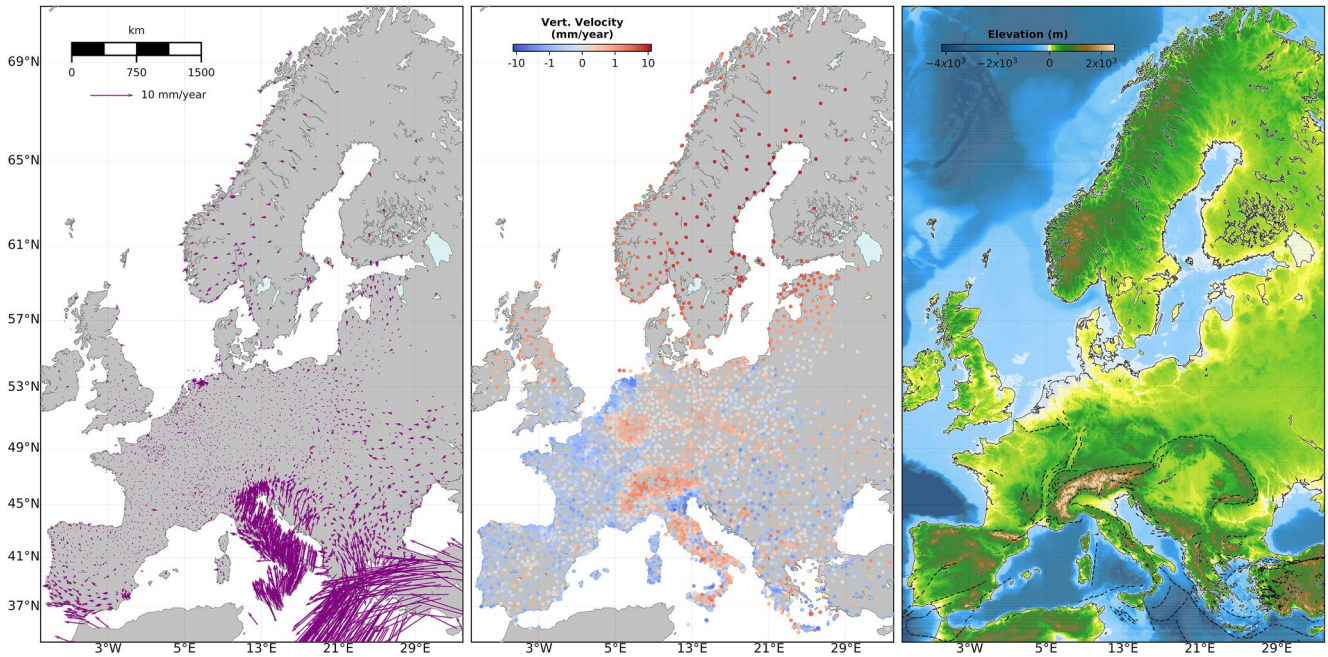

Figure 8. Horizontal (left) and vertical (center) smoothed velocity fields in Europe, derived from our analysis. The topography (Smith & Sandwell, 1997) and the main active tectonic structures are plotted on the right panel (Nocquet, 2012).

rate field in a local Cartesian coordinate system. In this system, x and y axes correspond to the two horizontal directions, the third axis z, corresponds to the vertical axis positive upward, and the corresponding displacement components are U, V, and W.

Since the available observations (GNSS velocities) are limited to the Earth surface, the observational data are $U(x, y, 0)$, $V(x, y, 0)$ and $W(x, y, 0)$ and the partial derivative of the surface displacement functions correspond to:

$$U'x = \frac{\partial U}{\partial x}; U'y = \frac{\partial U}{\partial y}; V'x = \frac{\partial V}{\partial x}; V'y = \frac{\partial V}{\partial y}; W'x = \frac{\partial W}{\partial x}; W'y = \frac{\partial W}{\partial y}$$

while $U'z$, $V'z$, $W'z$, are not available since there is no observation underneath the surface of the Earth.

The 3D strain rate components (ε) correspond to:

$$\varepsilon_{xx} = U'x; \varepsilon_{yy} = V'y; \varepsilon_{zz} = W'z$$

$$\varepsilon_{xy} = \frac{(U'x + V'x)}{2}; \varepsilon_{xz} = \frac{(U'z + W'x)}{2}; \varepsilon_{yz} = \frac{(V'z + W'y)}{2}$$

and, the second invariant of strain rate is defined as:

$$SSI = \sqrt{\varepsilon_{xx}{}^2 + \varepsilon_{yy}{}^2 + \varepsilon_{zz}{}^2 + 2 * \varepsilon_{xy}{}^2 + 2 * \varepsilon_{xz}{}^2 + 2 * \varepsilon_{yz}{}^2}$$

where ε_{zz} cannot be derived, while ε_{xz} and ε_{yz} can only be partially determined.

To estimate the 3D strain rate, assumptions must be done. At the surface of the Earth it can be considered that the stresses applied on the horizontal surface are null, that is, ss_{xz}, ss_{yz}, and ss_{zz} must be zero.

Assuming that the crust is a linear elastic material, we can use the Hooke's law and obtain:

$$ss_{xy} = \mu_0 * \varepsilon_{xz} = 0 \Rightarrow \varepsilon_{xz} = 0 \wedge U'z = -W'x$$

$$ss_{yz} = \mu_0 * \varepsilon_{yz} = 0 \Rightarrow \varepsilon_{yz} = 0 \wedge V'z = -W'y$$

$$ss_{zz} = \lambda * \varepsilon_{zz} + 2\mu_0 * (\varepsilon_{zz} + \varepsilon_{xx} + \varepsilon_{yy}) = 0 \Rightarrow \varepsilon_{zz} = \frac{-2\mu_0 * (\varepsilon_{xx} + \varepsilon_{yy})}{\lambda + 2\mu_0}$$

where λ and μ_0 correspond to the Lame constants. As a result, the second invariant of strain can be reduced to:

$$SSI_{3D} = \sqrt{{\varepsilon_{xx}}^2 + {\varepsilon_{yy}}^2 + 2 * {\varepsilon_{xy}}^2 + \left(\frac{-2\mu_0 * (\varepsilon_{xx} + \varepsilon_{yy})}{\lambda + 2\mu_0}\right)^2}$$

With those assumptions, the 3D second invariant of the deformation depends only on the horizontal velocities, since it is assumed that the vertical displacement can be predicted from the horizontal ones using elastic equations, which differs from the 2D case that is defined as follow:

$$SSI_{2D} = \sqrt{{\varepsilon_{xx}}^2 + {\varepsilon_{yy}}^2 + 2 * {\varepsilon_{xy}}^2}$$

Thus, taking values for the Lame constants for the Earth crust equal 60 Gpa for λ and μ_0 respectively, the differences of the second invariant of the strain rate tensor for 3D and 2D are negligible (Figure S8 in Supporting Information S1).

In order to obtain a robust and smoothed strain rate maps, an interpolation trade-off have been performed with VISR varying the weight threshold parameter w_t (see Shen et al. (2007) and Shen et al. (2015) for a complete explanation of the meaning of the Wt parameter) This parameter impacts the optimal distance considered by VISR to use or not a given GNSS velocity to interpolate the velocity field at each point of the grid. Larger values of this parameters generate smoother strain rate maps (Shen et al., 2015). A w_t value of 12 has been selected as this value generates the best velocity field interpolation. Figure S9 in Supporting Information S1 shows the distribution of the parameter D of the selected interpolation model ($w_t = 12$), that corresponds to the optimal interpolation distance for each coordinate, based on the in-situ data uncertainty and the density of GNSS data. For most of Europe this parameter remains stable at low values, suggesting that the chosen solution is stable for a wide region.

5. 3D Velocity Field, Strain Rates and Spatial Seismicity Distribution: Edge-Driven Deformation Versus Buoyancy-Driven of the Crust

5.1. Main Features of Our Combined Velocity Field and Derived Strain Rates

The resulting 3D velocity field with respect to stable Europe and the strain rates derived from it show characteristic patterns of known features in Europe (Figures 8, 9, and S7 in Supporting Information S1) (Grenerczy et al., 2000; Kenyeres et al., 2019; Nocquet, 2012; Nocquet & Calais, 2003, 2004).

With respect to stable Europe, a north-eastward movement is visible in the Italian peninsula and is associated to the movement of the Adria plate with respect to stable Europe. In southern Italy, Sicilia is moving toward the NNW at a rate of ∼5 mm/year with respect to stable Europe and is often considered as part of the Nubian plate. Instead, velocities point toward the NNE in Calabria that is often considered as the Apulia microplate. In central Italy, ∼3 mm/year of NE-SW extension associated with 1–2 mm/year of uplift characterizes the deformation along the range of the Apennines (D'Agostino et al., 2001; D'Agostino et al., 2008; D'Agostino et al., 2011; Devoti et al., 2017; Serpelloni et al., 2005). This north-eastward movement vanishes in the Dinarides and the Pannonian basin (D'Agostino et al., 2020; Métois et al., 2015), where the ∼3 mm/year convergence between Adria/Apulia and stable Europe is accommodated. A close look at the strain rate map in Figure 9 shows a transition from transtensive deformation mode and ∼1 mm/year subsidence in the north western coastal region of Croatia (Kvarner region) to a NNE-SSW compression and sub-millimeter uplift inland or further south in Dalmatia, Bosnia and Montenegro. Velocities rotate clockwise (Figure 9) around a pole located at the junction between the Dinarides and the Southern Balkans (D'Agostino et al., 2020; Métois et al., 2015). The areas affected by this clockwise rotation of the velocities are associated with a transpressive regime evolving into transtension and 0.5–1 mm/year uplift in the southern Balkans (42°N, 20–25°E). Velocities then display a large south-westward movement in the Aegean (Armijo et al., 2004; Cocard et al., 1999; Kreemer & Chamot-Rooke, 2004; Le Pichon et al., 1995; Nyst & Thatcher, 2004; Reilinger et al., 2010). As expected by previous knowledge of the deformation of the area, the strongest strain rate values are concentrated along the North Anatolian right-lateral strike-slip fault and across the Corinth Gulf that accommodates the N-S extension between Peloponnesus and continental Greece.

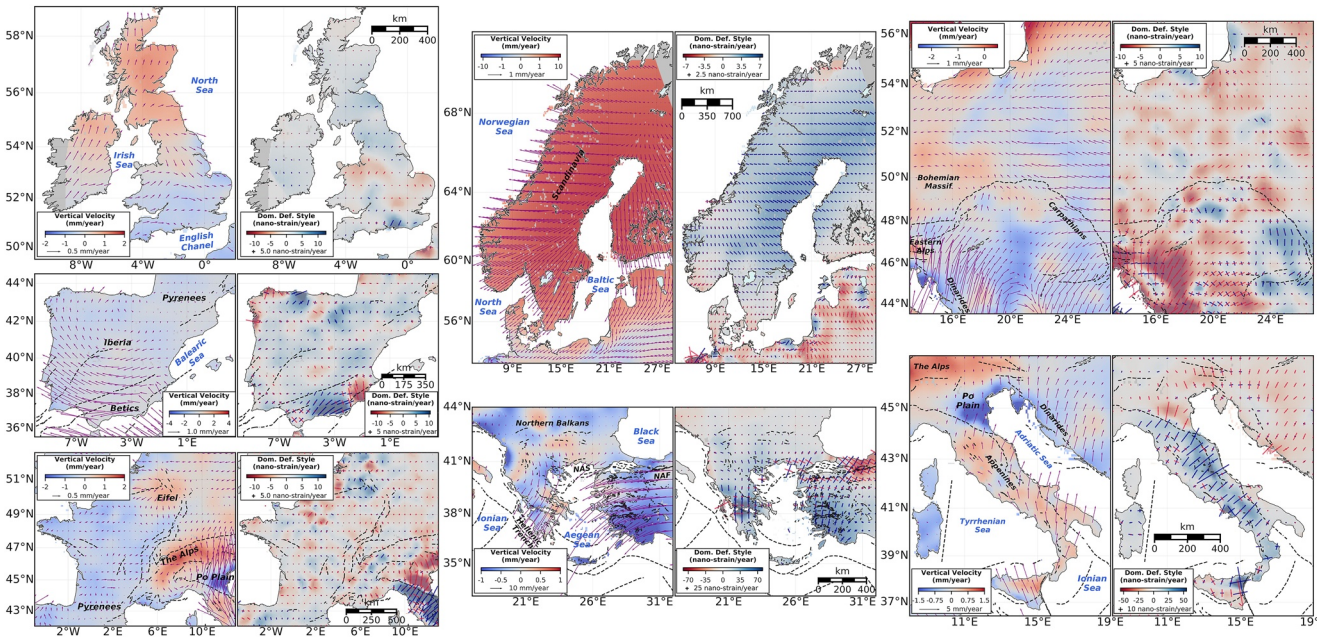

Figure 9. Close views of the interpolated vertical and horizontal velocity fields, and of the strain rate tensors and deformation style (extension in red and compression in blue). Main tectonic structures are shown as dashed lines. *Left column*: zoom on UK (top), Spain (center), France and Alps (bottom). *Center column*: zooms on Scandinavia (top) and the Balkans and the Aegean (bottom). *Right Column*: zoom on east Europe (top), and Italy (bottom).

In the westernmost part of the Mediterranean Sea, in the Betic Cordillera and the Rif, a westward movement of ~3–4 mm/year with respect to stable Europe generates a right-lateral strike slip deformation and the clockwise rotation of mainland Spain (Figure 9) associated with the extension of the Alboran domain as a response to the subduction rollback (Borque et al., 2019; Echeverria et al., 2013; Koulali et al., 2011; Vernant et al., 2010).

In Scandinavia, as a result of glacial isostatic adjustment, a strong vertical uplift centered on central Scandinavia, that locally exceeds 10 mm/year, is associated with a divergent horizontal velocity field that generates a NW-SE extension (Johansson et al., 2002; Lidberg et al., 2007; Nocquet et al., 2005). The uplifted zone extends beyond Scandinavia until Estonia, Latvia, Lithuania, the southern shore of the Baltic sea, Denmark, and reaches Scotland and Ireland to the westernmost. The areas surrounding the uplift zone are generally affected by a compressive regime.

In the Alps, our combined vertical velocity field confirms a ~2 mm/year uplift along the Alpine arc that extends from western Alps until the central Alps in Austria, with an uplift peak reaching 2.5 mm/year (Calais et al., 2002; Nocquet et al., 2016; Serpelloni et al., 2016; Walpersdorf et al., 2018). The strain rate field is characterized by a compression perpendicular to the range direction along both fronts of the Alps, that surround the area of the highest reliefs where extension is dominating. In the western Alps, the horizontal velocities are infra-millimetric, showing a movement compatible with right-lateral strike-slip, and an anticlockwise vorticity centered on the Po plain. In the central and eastern Alps, the ~2 mm/year convergence between the Adria plate and stable Europe is accommodated. The strain rates are characterized by a shortening of ~5–10 nanostrain/year in N-S direction, mostly localized along the southern front in the Dolomites, in Slovenia and northern Italy. To the north, the Bohemian Massif and the Cheb Basin—Eger rift (50°E, 14°N, Czech Republic) are affected by an uplift of ~1 mm/year. A sub-millimetric uplift extends to the East to the Carpathians, and surrounds the Pannonian basin (~46°N, 21°E) that is subsiding at ~1 mm/year. The uplifting area extends south down to the Balkans. Along the northern shore of the Black Sea, the Moesian platform (~45°N, 27°E) is affected by ~1 mm/year subsidence that transforms to the east into a few mm/year of uplift in the Ukrainian shield, once the Tornquist Suture is passed.

Central Europe, France, UK and Spain are characterized by very low velocities (0.1–1 mm/year), within the error bar. However, our outlier identification procedure, associated with the spatial filtering of the velocities allows to characterize the main direction of strain rates, the vertical movements, as well as the tectonic style. In both the

vertical and the horizontal, a clear local feature characterized by ~0.5–1 mm/year of uplift and a similar amount of radial velocity divergence is associated with the Eifel hotspot, located at the boundary between Belgium and Germany (with a centroid at ~50.5°N and 6.5°E), already highlighted by Kreemer et al. (2020). The other known hotspot discussed by Kreemer et al. (2020) is located in the French Massif Central (~45.5°N, 2.5°E). There, our results show null vertical velocities along a NW-SE diagonal that follows the South Armorican Shear Zone and the SW limit of the Hercynian Central Massif, while the surrounding areas are slowly subsiding at a rate of ~0.5 mm/year, which is compatible with Kreemer et al. (2020) and Masson et al. (2019b) results. The oriental Pyrenees are also characterized by a small uplift compared to the surroundings, and the whole Pyrenean chain is characterized by an NNE-SSW extension with a variable amount of strike-slip.

5.2. Toward a Separation of the Mechanisms Responsible for Deformation and Seismicity

In Europe, Italy and the Hellenic subduction present the largest seismicity rates of the continent, and are associated with large horizontal tectonic movements relative to stable Europe. On the other hand, stable regions (where low strain rates exist) usually exhibit low seismicity rate with earthquakes of low or moderate magnitude. Several attempts to relate strain and seismicity rates have been explored with relatively good results (that is, D'Agostino, 2014), especially on regions where horizontal strain rates associated with identified active faults are important. However, in regions of low strain rates that display non-negligible seismic activity, such as Fennoscandia or the Alps, the seismicity does not seem to be associated with the horizontal edge-driven strain rates but rather with the buoyancy-driven engendered by the isostatic adjustment and mantellic flow concomitant with the post-glacial rebound.

Assuming an elastic behavior for the crust and considering that the strike-slip deformation is negligible (i.e., principal stress component ss_2 is close to horizontal), the vertical movements in the crust can be separated in two parts: (a) the vertical deformation (thinning or thickening) generated by the horizontal tectonic compression or extension, and (b) the vertical movements generated by flexural deformation, spawned by the isostatic adjustments (e.g., post-glacial rebound) or the mantellic buoyancy (e.g., dynamic topography).

Horizontal velocity gradients generate strain rate components in the three directions ($\frac{\partial U}{\partial x}$, $\frac{\partial U}{\partial y}$, $\frac{\partial V}{\partial x}$, $\frac{\partial V}{\partial y}$, $\frac{\partial W}{\partial x}$, $\frac{\partial W}{\partial y}$), including in the vertical direction associated with thickening or thinning of the crust/lithosphere in response to tectonic horizontal compression or extension. Part of this thickness variation is instantaneously accommodated by isostasy, thus assuming that the horizontal strain rates is accommodated evenly over the crust thickness. The vertical velocity at the surface (H_S) associated with horizontal strain rates can be estimated using the expression proposed by Howell et al. (2017), modified for emerged lands:

$$H_S \simeq \frac{-T_l \left[(\rho_m - \rho_c) \frac{T_c}{T_l} \left(1 - \alpha\, t_1 \frac{T_c}{2T_l} \right) - \frac{\alpha\, t_1 \rho_m}{2} \right] (\varepsilon_1 + \varepsilon_2)}{\rho_m\, (1 - \alpha\, t_1)}$$

were T_c and T_l represent the thickness of the crust and the lithosphere respectively, ρ_m and ρ_c are the mantle and crust densities respectively, α corresponds to the volumetric coefficient of thermal expansion of the crust and the mantle, and t_1 is temperature of the asthenosphere. In order simplify the model, the effects of the thermal expansion can been neglected setting the α coefficient to zero, thus the equation presented above can be reduced to the following expression (corresponding to an incompressible crust, with an isostatically compensated thickening):

$$H_S \simeq \frac{-T_c\, (\varepsilon_1 + \varepsilon_2)\, (\rho_m - \rho_c)}{\rho_m}$$

Using this equation, considering an average crust thickness of 35 km for the whole region in order to keep the model simple, and assuming values of 2,700 and 3300 kg/m^3 for crust and mantle densities, a theoretical vertical velocity field due to horizontal strain rate can be derived (Figure 10—left). As expected, predictions of uplift and subsidence are controlled by the style of horizontal strain rates: in regions where extension dominates (such as in the central Apennines, the Corinth Gulf or the Balkans) subsidence is predicted, while in regions where the compression is dominant (e.g., eastern Alps, Dinarides) uplift if predicted.

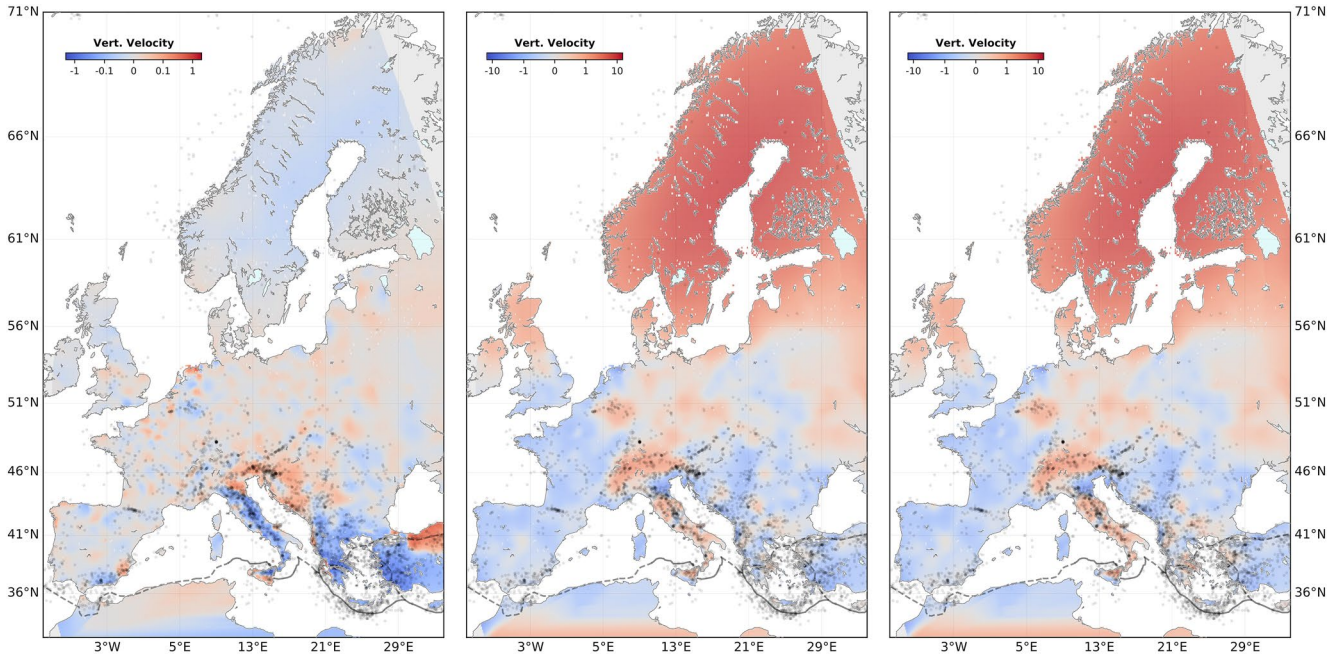

Figure 10. *Left*—Theoretical vertical velocity field in Europe derived from horizontal strain rates assuming a simple model of isostatic compensation. Blue and red colors represent regions of subsidence and uplift respectively. *Center*—Interpolation of the observed vertical velocity field. *Right*—Vertical movements associated with buoyancy-driven flexure (i.e., caused by isostatic adjustment or mantellic flow), obtained by computing the difference between the observed vertical velocity field and the one predicted by Howell et al. (2017) modified equation. Note that the color scale is logarithmic to highlight the abrupt fast changes of the vertical velocities behavior occurring in Europe.

As shown in Figure 10, the interpolation of the observed vertical velocity field and the predicted vertical velocity field computed from horizontal strain rates differ strongly. This suggests that a significant part of the observed vertical deformation can not be explained by elastic bulk deformation triggered by horizontal stress and therefore do not result in crustal thinning/thickening processes, but rather arise from deeper buoyancy-driven processes in the mantle. To image the regions of Europe most affected by the crust flexure, the contribution of the horizontal deformation to the observed vertical velocity field has been removed by differentiating the observed and the predicted vertical velocity fields (Figure 10—right). The regions that are most affected by buoyancy-driven vertical movements are: the Fennoscandia where Glacial Isostatic Adjustment is going on, Italy and the Aegean that are affected by a large-scale uplift generated by active mantellic upwelling (D'Agostino et al., 2001; Komut et al., 2012), the Alps where uplift results from isostatic adjustment combining effects of erosion, post-glacial rebound and delamination (Nocquet et al., 2016; Sternai et al., 2019), the Eifel hotspot and the Eger Cenozoic rift in the Bohemian massif where the active uplift may result either from a plume or from a mantellic upwelling (Plomerová et al., 2007; Plomerová et al., 2016), and the Ukrainian shield.

To appreciate the role of these two end-member driving processes (edge vs. buoyancy forces) on the generation of seismicity in Europe, an earthquake rate model (Figure 11—left) has been derived using the earthquake catalog used in the European Seismic Hazard Model ESHM13 (Grünthal et al., 2013; Stucchi et al., 2013; Woessner et al., 2015) and based on the methodology proposed by Hiemer et al. (2014), smoothing the earthquake source locations without considering seismogenic faults. The spatial distribution of the smoothed seismicity is then compared to the strain rate map (Figure 11—center), to the vertical velocity field associated with buoyancy (Figure 10—right), and to its horizontal gradient (Figure 11—right). For example, in the Southwestern Alps, where horizontal strain rates are low, the seismicity seems to be well correlated with the horizontal gradient of the vertical velocity field (Figure 11—right), suggesting that the seismicity of the region could be associated with the buoyancy-driven deformation of the lithosphere.

To evaluate more precisely the similarities between the earthquake rate model, the 2nd invariant of strain rate and the effect of crustal buoyancy-driven deformation (i.e., the interpolated vertical velocity field from which

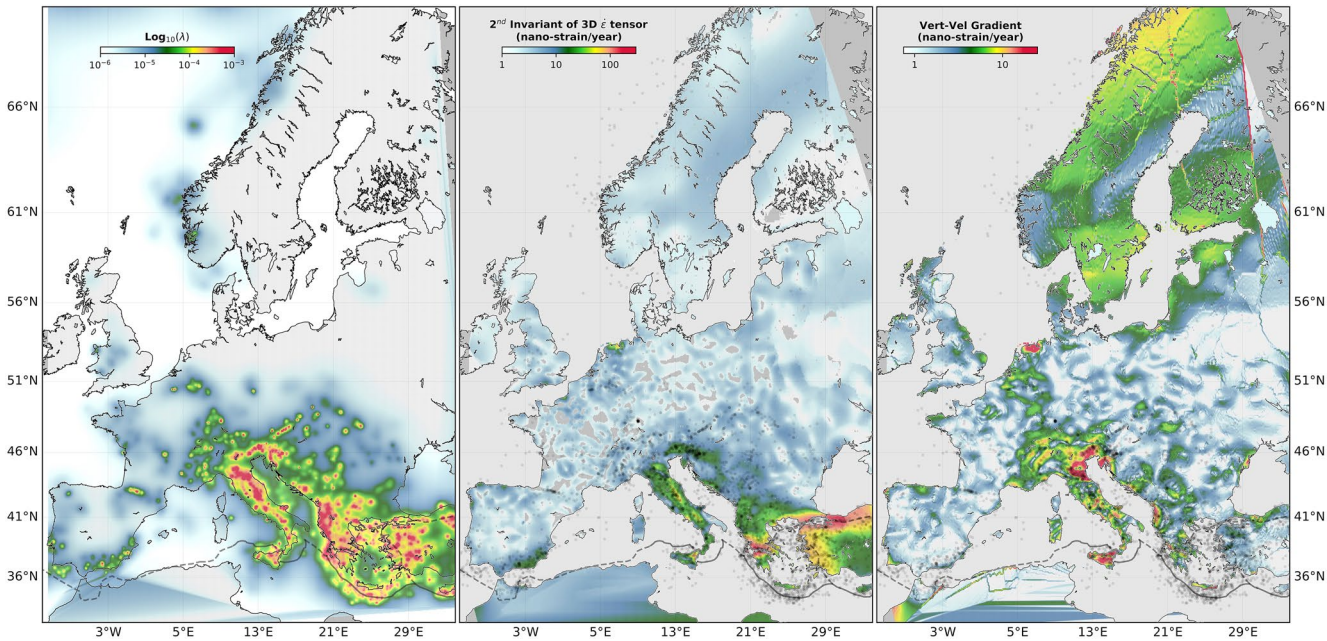

Figure 11. Left—Spatial distribution of cumulative annual earthquake rates (Mw > 4.5), based on the ESHM13 earthquake catalog and the Hiemer et al. (2014) smoothing algorithm. Center—Strain rate map superimposed on the seismicity of the earthquake catalog (gray dots), note that areas where the formal uncertainty on shear strain rate (see Figure S9 in Supporting Information S1) is larger than the 2nd invariant of the strain rate tensor, are masked. Right—Horizontal gradient of the flexural contribution of the interpolated vertical velocity superimposed on the seismicity of ESHM13 earthquake catalog (gray dots) (Woessner et al., 2015).

the plane-stress contribution has been removed, Figure 10-right and its horizontal derivative Figure 11-right), normalized correlation maps have been computed between pairs of images, in a squared sliding window:

$$c = \frac{\sum_{i,j=1}^{n} \left|\left(x_{ij} - \overline{x}\right) * \left(y_{ij} - \overline{y}\right)\right|}{n^2 * \sqrt{\sigma_x * \sigma_x}}$$

where c represents the correlation coefficient, x_{ij} and y_{ij} correspond to the fields values at position i,j on each sliding window. $\overline{x}$ and $\overline{y}$ are the mean values in the sliding window, n^2 the size of the square sliding window, and σ_x and σ_y is the standart deviation of values in the sliding window. Then the absolute value of the correlation coefficient is assigned to the center of the sliding window.

The correlation maps obtained using this method are sensitive to the size of the sliding window, and several window sizes allow to highlight processes of different characteristic wavelengths. For example, the deformation and the seismicity distributions in the southern part of Europe (mostly controlled by boundary forces associated with horizontal plates movements, i.e., edge-driven) present patterns of smaller wavelength than in northern Europe (mostly dominated by post-glacial adjustment and generating a broad signal). Taking this limitation into account, we examine the correlations between the smoothed seismicity and the strain rate, the flexure contribution to the vertical displacements, or its horizontal gradient using a window of 0.75° (Figure 12).

In northern Europe, although Scandinavia is affected by the largest vertical rates due to GIA, the correlation pattern observed is not obvious because the seismicity is located mostly offshore and because the deformation is well constrained on the continents only. More, the large wavelength of the deformation field in Scandinavia necessarily implies a small maximum correlation value. Still, the maximum of correlation with seismicity is found along the NW coast of Norway for both the horizontal gradient of vertical deformation and the vertical velocity field suggesting that the seismicity there might be a response to the flexure generated by the post-glacial adjustment.

In other areas of stable plate interiors characterized by a low horizontal deformation (i.e., 2nd invariant of strain rates lower or equal to ~10 nanostrain/year), four areas exhibit a quite important seismicity rate:

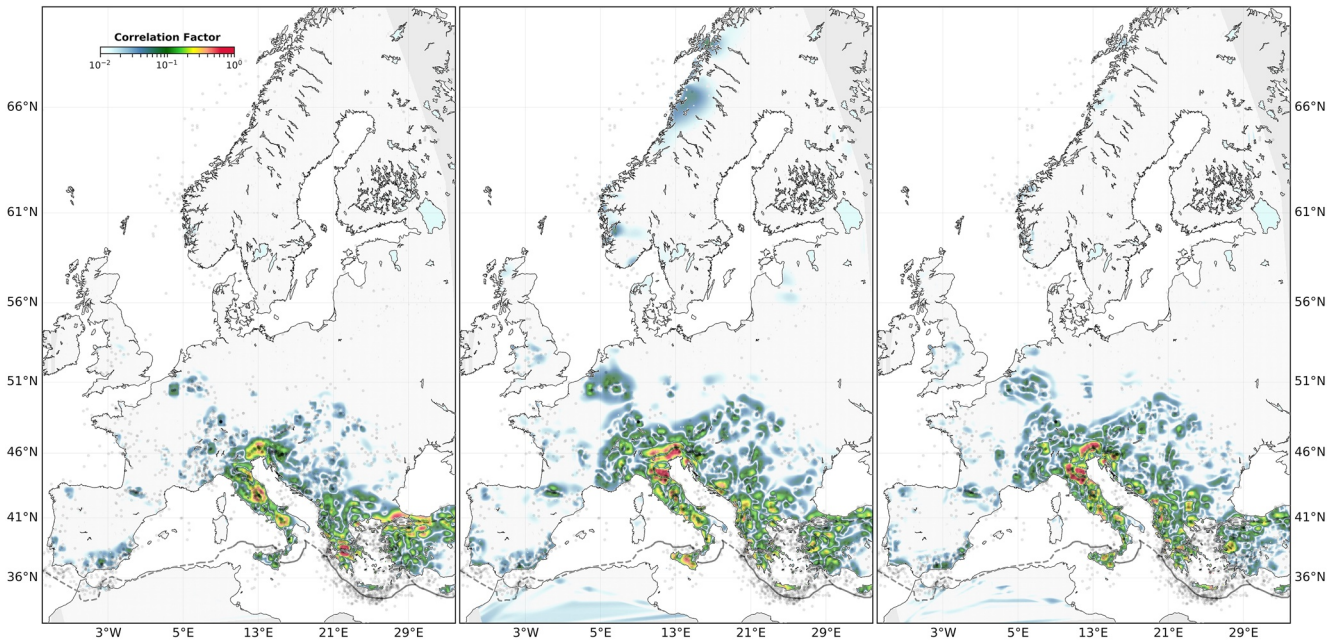

Figure 12. Normalized correlation maps, computed using a sliding window of 0.75°, between spatial distribution of cumulative annual earthquake rates and the 2nd invariant of strain Rates (left), Vertical velocity field due to buoyancy-driven (center), or the Horizontal gradient of the vertical velocity due to buoyancy-driven (right).

1. The Alps.
2. The Eifel volcanic area.
3. The Carpathian.
4. The Pyrenees.

The correlation maps obtained for these regions show that only a small portion of the seismicity distribution is well correlated with horizontal tectonic deformation. The Northwestern Alps (close to the Leman Lake) and the Eifel volcanic region are characterized by moderate strain rates and important vertical uplift. There, the seismicity is best correlated with the vertical velocity field, suggesting a prevalence of buoyancy-induced mantel processes in controlling deformation and seismicity in those areas. In the Carpathian, even if the uplift is less important, the seismicity correlates well with vertical uplift and its horizontal gradient, suggesting that the seismicity could be associated with flexure. In the Pyrenees, affected by NE-SW extension (Figure 9) (Rigo et al., 2015) and limited relative uplift (Figure 9) (Masson et al., 2019b), a strong seismic activity occurs in the area of Lourdes. It is well correlated with the horizontal gradient of the vertical displacements (Figure 12), suggesting that the mechanism that controls the seismicity in this area might be the flexure, or gravitational collapse of the mountain chain during the isostatic upwelling of the orogenic crust (Lukk & Shevchenko, 2018). Similarly, the smoothed seismicity rates and the horizontal gradient of the vertical displacement associated to flexure correlate well in the Southwestern Alps.

The southern part of the Iberic Peninsula (Betic cordillera), the Corinth rift in Greece, and the North Anatolian Fault all show a good correlation with the 2nd invariant of strain rate, suggesting that the seismicity is there mainly controlled by the tectonic processes (edge-driven, i.e., result of tractions at plate boundaries) generating mostly horizontal deformation (and associated bulk vertical deformation). Along the Apennines in Central Italy, the seismicity seems to be well correlated with the 2nd invariant of strain rates, but also with the vertical uplift that affects the area, suggesting that the seismicity might result from both edge and buoyancy-driven, that is, both "edge-driven" (result of tractions at plate boundaries) and "mantle-driven." In Sicilia, a correlation is found with vertical only suggesting that volcanism might be the main driving process there. Finally, in Northern Italy and along the southern front of the Eastern Alps (Emilia-Romagna, Dolomites), a strong correlation is found with the horizontal gradient of the vertical displacement, suggesting that the flexure of the Adriatic plate as a response to its subduction below stable Europe might be the dominant mechanism there.

In the Balkans, the distribution of seismicity ressembles the strain rate distribution. Still, best correlations are found with the vertical velocity field, which suggest a complex interaction between the effects of the mantellic buoyancy and the edge-driven tectonics to explain the seismicity.

6. Conclusion

The combination of different GNSS velocity solutions and the proposed filtering process are efficient tools to generate a dense 3D velocity field covering the whole Europe (Figures 8, 9, and S7 in Supporting Information S1), allowing to study the processes responsible for the large-scale deformation. The outliers and scatter in the velocities could be mitigated by applying a proper filtering and smoothing strategy, and provided reliable results even in slowly deforming areas. Most of the features of the 3D velocity field, strain rate and rotation maps detected by previous works in Europe are clearly visible, within a wide range of GNSS velocity amplitudes.

The strain rate maps derived from the GNSS velocity field show a good agreement with the seismicity in regions that experience important tectonic deformation, but cannot explain the seismicity in regions with important vertical velocities, such as regions affected by post glacial rebound, dynamic topography and mantle buoyancy processes, or other isostatic processes that induce flexure on the lithosphere. Using a simple model of vertical motion driven by crustal compensation of topography created by horizontal deformation, we could predict the theoretical vertical displacement associated with horizontal convergent or divergent fields. This prediction has then been subtracted from the measured vertical velocity field to map the regions that undergo the effects of buoyancy forces (Figure 10).

A smoothed seismicity rate model has been derived from the declustered earthquake catalog used in the European Seismic Hazard Model ESHM13 (Woessner et al., 2015) (Figure 11 left), and compared to the obtained deformation maps. A good correlation (Figure 12) is usually found between the smoothed seismicity rate and the strain rate in regions dominated by the edge-driven horizontal tectonics, such as the North Anatolian Fault, the Corinth rift in Greece, or the southern part of Spain (Betic cordillera) (D'Agostino, 2014; Métois et al., 2015). In the regions that experience significant vertical velocities that cannot be explained by edge-driven horizontal tectonic forces, such as the Central Alps, the Eifel Volcanic region, the Pyrenees or some areas of Central Europe, the strain rate does not correlate with the seismicity that may rather be generated by vertical flexure of the crust induced by isostasy or mantle dynamics (e.g., Brandes et al., 2019; Keiding et al., 2015; Walpersdorf et al., 2018). In regions such as the Apennines, the Balkans, or the Eastern Alps, the seismicity seems to be influenced by both processes.

The correlation between the smoothed seismicity rate and markers such as the vertical velocity field or its horizontal gradient suggests that the flexure of the crust plays a more important role than previously thought on the generation of seismicity. An important part of the intracontinental seismicity in Europe is located around regions that undergo uplift, or at the transition between uplift and subsidence, such as around the Alpine arc or in northern Italy, where the horizontal gradients of the vertical velocities are higher. Those observations are consistent with the strain rates induced by flexural deformation that generates surface extension in uplifted areas, shortening in areas of subsidence and concentrates shear stresses in zones of high horizontal gradient of vertical velocity (Couples et al., 1998) due to isostasy or mantellic processes (Faccenna et al., 2014; Gvirtzman et al., 2016). Whereas those effects are considered as second order stresses for regions of large horizontal strain rates, they could control the crustal seismicity in zones of low tectonic deformation (Tarayoun et al., 2018), such as in the volcanic Eifel zone (Kreemer, 2020) or in the Alps.

Also, in regions with significant vertical movements and complex structural inheritance, such as the Alps, the Pyrenees or the Eger rift in the Bohemian massif, the role of the buoyancy-driven processes on the local seismicity rate can be important (Mazzotti et al., 2020; Tarayoun et al., 2018). Even in a region with an important contribution of edge-driven processes like Italy or the northern Balkans, the high rates of vertical deformation could have an important impact on the seismicity, implying a considerable impact for seismic hazard. We emphasize that, in addition to the horizontal strain rate, the vertical deformation of isostatic or mantellic origin must be considered as an important input to hazard models in Europe.

Data Availability Statement

All individual Global Navigation Satellite System (GNSS) velocity field solutions are online available: EPOS-UGA solution is available at https://www.isterre.fr/english/research-observation/research-projects/european-projects/article/epos-gnss-products.html, NGL solution is available at http://geodesy.unr.edu, ETH solution is available at https://doi.pangaea.de/10.1594/PANGAEA.886889, MONT solution is available at https://data.oreme.org/doi/view/2cdc72ec-1066-486c-aef7-9da36662f46d, KIER solution is available at https://doi.org/10.1016/j.jog.2021.101845, KIER solution is available as supplementary material at https://www.sciencedirect.com/science/article/pii/S0264370721000314?via%3Dihub, CEUR solution is available at http://cegrn.cisas.unipd.it/CEGRN/network/CEG_tableVEL.htm, KREE solution is available at https://dataverse.harvard.edu/dataset.xhtml?persistentId=doi:10.7910/DVN/ONATFP, BALK solution is available as supplementary material at https://www.sciencedirect.com/science/article/pii/S0012821X20301898#se0090, EPND solution is available at https://epnd.sgo-penc.hu/downloads/ and INGV solution that has been provided through personal communication by the author. The code used to combined and transform the GNSS velocity fields is rotvel, a package distributed with the GAMIT/GLOBK suite.

Acknowledgments
This research project has received funding from the European Union's Horizon 2020 research and innovation program, for the SERA project under grant agreement No 730900. This work has been performed in the frame of Rénag and EPOS (European Plate Observing System). Rénag is member of the Research Infrastructure (RI) Résif-Epos, managed by CNRS-Insu. Résif-Epos benefits from the support of the Ministry of Ecological Transition and RESIF-CORE (Convention No ANR-11-EQPX-0040). ORPHEON GNSS data were provided to the authors for a scientific use in the framework of the GEODATA-INSU-CNRS convention.

References

Altamimi, Z., Collilieux, X., & Métivier, L. (2011). ITRF2008: An improved solution of the international terrestrial reference frame. *Journal of Geodesy*, *85*(8), 457–473. https://doi.org/10.1007/s00190-011-0444-4

Altamimi, Z., Métivier, L., Rebischung, P., Rouby, H., & Collilieux, X. (2017). ITRF2014 plate motion model. *Geophysical Journal International*, *209*(3), 1906–1912. https://doi.org/10.1093/gji/ggx136

Altamimi, Z., Rebischung, P., Métivier, L., & Collilieux, X. (2016). ITRF2014: A new release of the International Terrestrial Reference Frame modeling nonlinear station motions. *Journal of Geophysical Research: Solid Earth*, *121*(8), 6109–6131. https://doi.org/10.1002/2016jb013098

Altamimi, Z., Sillard, P., & Boucher, C. (2002). ITRF2000: A new release of the International Terrestrial Reference Frame for Earth science applications. *Journal of Geophysical Research*, *107*(B10). ETG 2-1-ETG 2-19. https://doi.org/10.1029/2001JB000561

Altamimi, Z., Sillard, P., & Boucher, C. (2007). *CATREF software: Combination and analysis of Terrestrial Reference frames*. LAREG Technical, Institut Géographique National.

Armijo, R., Flerit, F., King, G., & Meyer, B. (2004). Linear elastic fracture mechanics explains the past and present evolution of the Aegean. *Earth and Planetary Science Letters*, *217*(1), 85–95. https://doi.org/10.1016/S0012-821X(03)00590-9

Bertiger, W., Bar-Sever, Y., Dorsey, A., Haines, B., Harvey, N., Hemberger, D., et al. (2020). GipsyX/RTGx, a new tool set for space geodetic operations and research. *Advances in Space Research*, *66*(3), 469–489. https://doi.org/10.1016/j.asr.2020.04.015

Blewitt, G., Hammond, W. C., & Kreemer, C. (2018). Harnessing the GPS data explosion for interdisciplinary science. *Eos*, *99*, 1–2. https://doi.org/10.1029/2018EO104623

Blewitt, G., Kreemer, C., Hammond, W. C., & Gazeaux, J. (2016). MIDAS robust trend estimator for accurate GPS station velocities without step detection. *Journal of Geophysical Research: Solid Earth*, *121*(3), 2054–2068. https://doi.org/10.1002/2015jb012552

Borque, M. J., Sanchez-Alzola, A., Martin-Rojas, I., Alfaro, P., Molina, S., Rosa-Cintas, S., et al. (2019). How much Nubia-Eurasia convergence is accommodated by the NE end of the Eastern Betic Shear Zone (SE Spain)? Constraints from GPS velocities. *Tectonics*, *38*(5), 1824–1839. https://doi.org/10.1029/2018TC004970

Bos, M. S., Fernandes, R. M. S., Williams, S. D. P., & Bastos, L. (2008). Fast error analysis of continuous GPS observations. *Journal of Geodesy*, *82*(3), 157–166. https://doi.org/10.1007/s00190-007-0165-x

Brandes, C., Plenefisch, T., Tanner, D. C., Gestermann, N., & Steffen, H. (2019). Evaluation of deep crustal earthquakes in northern Germany – Possible tectonic causes. *Terra Nova*, *31*(2), 83–93. https://doi.org/10.1111/ter.12372

Bruyninx, C., Habrich, H., Söhne, W., Kenyeres, A., Stangl, G., & Völksen, C. (2012). *Enhancement of the EUREF permanent network services and products*. paper presented at Geodesy for Planet Earth.

Calais, E., Nocquet, J.-M., Jouanne, F., & Tardy, M. (2002). Current strain regime in the Western Alps from continuous Global Positioning System measurements, 1996–2001. *Geology*, *30*(7), 651–654. https://doi.org/10.1130/0091-7613(2002)030<0651:Csritw>2.0.Co;2

Cocard, M., Kahle, H. G., Peter, Y., Geiger, A., Veis, G., Felekis, S., et al. (1999). New constraints on the rapid crustal motion of the Aegean region: Recent results inferred from GPS measurements (1993–1998) across the West Hellenic Arc, Greece. *Earth and Planetary Science Letters*, *172*(1), 39–47. https://doi.org/10.1016/S0012-821X(99)00185-5

Couples, G. D., Lewis, H., & Geoff Tanner, P. W. (1998). Strain partitioning during flexural-slip folding. *Geological Society, London, Special Publications*, *127*(1), 149–165. https://doi.org/10.1144/GSL.SP.1998.127.01.12

Dach, R., Lutz, S., Walser, P., & Fridez, P. (2015). *Bernese GNSS software version 5.2*. University of Bern, Bern Open Publishing. https://doi.org/10.7892/boris.72297

D'Agostino, N. (2014). Complete seismic release of tectonic strain and earthquake recurrence in the Apennines (Italy). *Geophysical Research Letters*, *41*(4), 1155–1162. https://doi.org/10.1002/2014gl059230

D'Agostino, N., Avallone, A., Cheloni, D., D'Anastasio, E., Mantenuto, S., & Selvaggi, G. (2008). Active tectonics of the Adriatic region from GPS and earthquake slip vectors. *Journal of Geophysical Research*, *113*(B12), B12413. https://doi.org/10.1029/2008JB005860

D'Agostino, N., Giuliani, R., Mattone, M., & Bonci, L. (2001). Active crustal extension in the Central Apennines (Italy) inferred from GPS measurements in the interval 1994–1999. *Geophysical Research Letters*, *28*(10), 2121–2124. https://doi.org/10.1029/2000GL012462

D'Agostino, N., Mantenuto, S., D'Anastasio, E., Giuliani, R., Mattone, M., Calcaterra, S., et al. (2011). Evidence for localized active extension in the central Apennines (Italy) from Global Positioning System observations. *Geology*, *39*(4), 291–294. https://doi.org/10.1130/g31796.1

D'Agostino, N., Métois, M., Koci, R., Duni, L., Kuka, N., Ganas, A., et al. (2020). Active crustal deformation and rotations in the southwestern Balkans from continuous GPS measurements. *Earth and Planetary Science Letters*, *539*, 116246. https://doi.org/10.1016/j.epsl.2020.116246

Davies, P., & Blewitt, G. (2000). Methodology for global geodetic time series estimation: A new tool for geodynamics. *Journal of Geophysical Research*, *105*(B5), 11083–11100. https://doi.org/10.1029/2000JB900004

Deprez, A., Socquet, A., Walpersdorf, A., Cotte, N., & Tarayoun, A. (2019). *GNSS position and velocity solutions in Europe (data)*. OSUG CNRS ISTERRE. https://doi.org/10.17178/GNSS

de Vicente, G., & Vegas, R. (2009). Large-scale distributed deformation controlled topography along the western Africa–Eurasia limit: Tectonic constraints. *Tectonophysics*, *474*(1), 124–143. https://doi.org/10.1016/j.tecto.2008.11.026

Devoti, R., D'Agostino, N., Serpelloni, E., Pietrantonio, G., Riguzzi, F., Avallone, A., et al. (2017). *A combined velocity field of the Mediterranean region* (p. S0215). Annals of Geophysics.

Echeverria, A., Khazaradze, G., Asensio, E., Gárate, J., Dávila, J. M., & Suriñach, E. (2013). Crustal deformation in eastern Betics from CuaTeNeo GPS network. *Tectonophysics*, *608*, 600–612. https://doi.org/10.1016/j.tecto.2013.08.020

Faccenna, C., Becker, T. W., Miller, M. S., Serpelloni, E., & Willett, S. D. (2014). Isostasy, dynamic topography, and the elevation of the Apennines of Italy. *Earth and Planetary Science Letters*, *407*, 163–174. https://doi.org/10.1016/j.epsl.2014.09.027

Grenerczy, G., Kenyeres, A., & Fejes, I. (2000). Present crustal movement and strain distribution in Central Europe inferred from GPS measurements. *Journal of Geophysical Research*, *105*(B9), 21835–21846. https://doi.org/10.1029/2000JB900127

Grünthal, G., Wahlström, R., & Stromeyer, D. (2013). The SHARE European Earthquake Catalogue (SHEEC) for the time period 1900–2006 and its comparison to the European-Mediterranean Earthquake Catalogue (EMEC). *Journal of Seismology*, *17*(4), 1339–1344. https://doi.org/10.1007/s10950-013-9379-y

Gvirtzman, Z., Faccenna, C., & Becker, T. W. (2016). Isostasy, flexure, and dynamic topography. *Tectonophysics*, *683*, 255–271. https://doi.org/10.1016/j.tecto.2016.05.041

Héroux, P., & Kouba, J. (2001). GPS precise point positioning using IGS orbit products. *Physics and Chemistry of the Earth - Part A: Solid Earth and Geodesy*, *26*(6), 573–578. https://doi.org/10.1016/S1464-1895(01)00103-X

Herring, T. A., King, R. W., & McClusky, S. C. (2018). *GAMIT reference manual (GNSS analysis at MIT)*. Massachussetts Institute of Technology.

Herring, T. A., Melbourne, T. I., Murray, M. H., Floyd, M. A., Szeliga, W. M., King, R. W., et al. (2016). Plate Boundary Observatory and related networks: GPS data analysis methods and geodetic products. *Reviews of Geophysics*, *54*(4), 759–808. https://doi.org/10.1002/2016RG000529

Hiemer, S., Woessner, J., Basili, R., Danciu, L., Giardini, D., & Wiemer, S. (2014). A smoothed stochastic earthquake rate model considering seismicity and fault moment release for Europe. *Geophysical Journal International*, *198*(2), 1159–1172. https://doi.org/10.1093/gji/ggu186

Howell, A., Jackson, J., Copley, A., McKenzie, D., & Nissen, E. (2017). Subduction and vertical coastal motions in the eastern Mediterranean. *Geophysical Journal International*, *211*(1), 593–620. https://doi.org/10.1093/gji/ggx307

Johansson, J. M., Davis, J. L., Scherneck, H. G., Milne, G. A., Vermeer, M., Mitrovica, J. X., et al. (2002). Continuous GPS measurements of postglacial adjustment in Fennoscandia 1. Geodetic results. *Journal of Geophysical Research*, *107*(B8), ETG 3-1-ETG 3-27. https://doi.org/10.1029/2001JB000400

Keiding, M., Kreemer, C., Lindholm, C. D., Gradmann, S., Olesen, O., & Kierulf, H. P. (2015). A comparison of strain rates and seismicity for Fennoscandia: Depth dependency of deformation from glacial isostatic adjustment. *Geophysical Journal International*, *202*(2), 1021–1028. https://doi.org/10.1093/gji/ggv207

Kenyeres, A., Bellet, J. G., Bruyninx, C., Caporali, A., de Doncker, F., Droscak, B., et al. (2019). Regional integration of long-term national dense GNSS network solutions. *GPS Solutions*, *23*(4), 122. https://doi.org/10.1007/s10291-019-0902-7

Kierulf, H. P., Steffen, H., Barletta, V. R., Lidberg, M., Johansson, J., Kristiansen, O., & Tarasov, L. (2021). A GNSS velocity field for geophysical applications in Fennoscandia. *Journal of Geodynamics*, *146*, 101845. https://doi.org/10.1016/j.jog.2021.101845

Komut, T., Gray, R., Pysklywec, R., & Göğüş, O. H. (2012). Mantle flow uplift of western Anatolia and the Aegean: Interpretations from geophysical analyses and geodynamic modeling. *Journal of Geophysical Research*, *117*(B11), B11412. https://doi.org/10.1029/2012JB009306

Koulali, A., Ouazar, D., Tahayt, A., King, R. W., Vernant, P., Reilinger, R. E., et al. (2011). New GPS constraints on active deformation along the Africa–Iberia plate boundary. *Earth and Planetary Science Letters*, *308*(1), 211–217. https://doi.org/10.1016/j.epsl.2011.05.048

Kreemer, C. (2020). *Replication data for: Geodetic evidence for a buoyant mantle plume beneath the Eifel volcanic area, NW Europe*. https://doi.org/10.7910/DVN/ONATFP

Kreemer, C., & Blewitt, G. (2021). Robust estimation of spatially varying common-mode components in GPS time-series. *Journal of Geodesy*, *95*(1), 13. https://doi.org/10.1007/s00190-020-01466-5

Kreemer, C., Blewitt, G., & Davis, P. M. (2020). Geodetic evidence for a buoyant mantle plume beneath the Eifel volcanic area, NW Europe. *Geophysical Journal International*, *222*(2), 1316–1332. https://doi.org/10.1093/gji/ggaa227

Kreemer, C., Blewitt, G., & Klein, E. C. (2014). A geodetic plate motion and Global Strain Rate Model. *Geochemistry, Geophysics, Geosystems*, *15*(10), 3849–3889. https://doi.org/10.1002/2014GC005407

Kreemer, C., & Chamot-Rooke, N. (2004). Contemporary kinematics of the southern Aegean and the Mediterranean ridge. *Geophysical Journal International*, *157*(3), 1377–1392. https://doi.org/10.1111/j.1365-246X.2004.02270.x

Legrand, J., Bergeot, N., Bruyninx, C., Wöppelmann, G., Santamaría-Gómez, A., Bouin, M. N., & Altamimi, Z. (2012). *Comparison of regional and global GNSS positions, velocities and residual time series, paper presented at geodesy for planet Earth*. Springer Berlin Heidelberg.

Legrand, J., & Bruyninx, C. (2009). EPN reference frame alignment: Consistency of the station positions. *Bulletin of Geodesy and Geomatics*, *68*(1), 19–34.

Le Pichon, X., Chamot-Rooke, N., Lallemant, S., Noomen, R., & Veis, G. (1995). Geodetic determination of the kinematics of central Greece with respect to Europe: Implications for eastern Mediterranean tectonics. *Journal of Geophysical Research*, *100*(B7), 12675–12690. https://doi.org/10.1029/95jb00317

Lidberg, M., Johansson, J. M., Scherneck, H.-G., & Davis, J. L. (2007). An improved and extended GPS-derived 3D velocity field of the glacial isostatic adjustment (GIA) in Fennoscandia. *Journal of Geodesy*, *81*(3), 213–230. https://doi.org/10.1007/s00190-006-0102-4

Lukk, A. A., Leonova, V. G., & Sidorin, A. Y. (2019). Revisiting the origin of seismicity in Fennoscandia. *Izvestiya - Atmospheric and Oceanic Physics*, *55*(7), 743–758. https://doi.org/10.1134/S000143381907003X

Lukk, A. A., & Shevchenko, V. I. (2018). Peculiarity of the Relationship between the Seismicity and Tectonic Structure of the Pyrenees. *Izvestiya - Physics of the Solid Earth*, *54*(3), 415–429. https://doi.org/10.1134/S1069351318030060

Masson, C., Mazzotti, S., Vernant, P., & Doerflinger, E. (2019a). Extracting small deformation beyond individual station precision from dense Global Navigation Satellite System (GNSS) networks in France and western Europe. *Solid Earth*, *10*(6), 1905–1920. Data providers and velocity field, OSU OREME. https://doi.org/10.5194/se-10-1905-2019

Masson, C., Mazzotti, S., Vernant, P., & Doerflinger, E. (2019b). Extracting small deformation beyond individual station precision from dense Global Navigation Satellite System (GNSS) networks in France and Western Europe. *Solid Earth*, *10*(6), 1905–1920. https://doi.org/10.5194/se-10-1905-2019

Mazzotti, S., Jomard, H., & Masson, F. (2020). Processes and deformation rates generating seismicity in metropolitan France and conterminous Western Europe. *BSGF - Earth Science Bulletin*, *191*, 19. https://doi.org/10.1051/bsgf/2020019

Métois, M., D'Agostino, N., Avallone, A., Chamot-Rooke, N., Rabaute, A., Duni, L., et al. (2015). Insights on continental collisional processes from GPS data: Dynamics of the peri-Adriatic belts. *Journal of Geophysical Research: Solid Earth*, *120*(12), 8701–8719. https://doi.org/10.1002/2015jb012023

Mörner, N.-A. (1991). Intense earthquakes and seismotectonics as a function of glacial isostasy. *Tectonophysics*, *188*(3), 407–410. https://doi.org/10.1016/0040-1951(91)90471-4

Mouslopoulou, V., Oncken, O., Hainzl, S., & Nicol, A. (2016). Uplift rate transients at subduction margins due to earthquake clustering. *Tectonics*, *35*(10), 2370–2384. https://doi.org/10.1002/2016tc004248

Nocquet, J.-M. (2012). Present-day kinematics of the Mediterranean: A comprehensive overview of GPS results. *Tectonophysics*, *579*, 220–242. https://doi.org/10.1016/j.tecto.2012.03.037

Nocquet, J.-M., & Calais, E. (2003). Crustal velocity field of western Europe from permanent GPS array solutions, 1996–2001. *Geophysical Journal International*, *154*(1), 72–88. https://doi.org/10.1046/j.1365-246X.2003.01935.x

Nocquet, J.-M., & Calais, E. (2004). Geodetic measurements of crustal deformation in the Western Mediterranean and Europe. *Pure and Applied Geophysics*, *161*(3), 661–681. https://doi.org/10.1007/s00024-003-2468-z

Nocquet, J.-M., Calais, E., Altamimi, Z., Sillard, P., & Boucher, C. (2001). Intraplate deformation in western Europe deduced from an analysis of the International Terrestrial Reference Frame 1997 (ITRF97) velocity field. *Journal of Geophysical Research*, *106*(B6), 11239–11257. https://doi.org/10.1029/2000JB900410

Nocquet, J.-M., Calais, E., & Parsons, B. (2005). Geodetic constraints on glacial isostatic adjustment in Europe. *Geophysical Research Letters*, *32*(6), L06308. https://doi.org/10.1029/2004GL022174

Nocquet, J.-M., Sue, C., Walpersdorf, A., Tran, T., Lenotre, N., Vernant, P., et al. (2016). Present-day uplift of the western Alps. *Scientific Reports*, *6*(1), 28404. https://doi.org/10.1038/srep28404

Nyst, M., & Thatcher, W. (2004). New constraints on the active tectonic deformation of the Aegean. *Journal of Geophysical Research*, *109*(B11), B11406. https://doi.org/10.1029/2003JB002830

Plomerová, J., Achauer, U., Babuška, V., Vecsey, L., & group, B. w. (2007). Upper mantle beneath the Eger Rift (Central Europe): Plume or asthenosphere upwelling? *Geophysical Journal International*, *169*(2), 675–682. https://doi.org/10.1111/j.1365-246X.2007.03361.x

Plomerová, J., Munzarová, H., Vecsey, L., Kissling, E., Achauer, U., & Babuška, V. (2016). Cenozoic volcanism in the Bohemian Massif in the context of P- and S-velocity high-resolution teleseismic tomography of the upper mantle. *Geochemistry, Geophysics, Geosystems*, *17*(8), 3326–3349. https://doi.org/10.1002/2016GC006318

Rebischung, P. (2012). *IGb08: An update on IGS08*. International GNSS Service. Retrieved from http://igscb.jpl.nasa.gov/pipermail/igsmail/2012/006655

Reilinger, R., McClusky, S., Paradissis, D., Ergintav, S., & Vernant, P. (2010). Geodetic constraints on the tectonic evolution of the Aegean region and strain accumulation along the Hellenic subduction zone. *Tectonophysics*, *488*(1), 22–30. https://doi.org/10.1016/j.tecto.2009.05.027

Rigo, A., Vernant, P., Feigl, K. L., Goula, X., Khazaradze, G., Talaya, J., et al. (2015). Present-day deformation of the Pyrenees revealed by GPS surveying and earthquake focal mechanisms until 2011. *Geophysical Journal International*, *201*(2), 947–964. https://doi.org/10.1093/gji/ggv052

Rosenbaum, G., Lister, G., & Duboz, C. (2002). Reconstruction of the tectonic evolution of the western Mediterranean since the Oligocene. *Journal of the Virtual Explorer*, *8*, 107–126. https://doi.org/10.3809/jvirtex.2002.0039

Sánchez, L., Drewes, H., Brunini, C., Mackern, M. V., & Martínez-Díaz, W. (2016). *SIRGAS core network stability*. Springer International Publishing. paper presented at IAG 150 Years.

Sánchez, L., Völksen, C., Sokolov, A., Arenz, H., & Seitz, F. (2018a). Present-day surface deformation of the Alpine region inferred from geodetic techniques. *Earth System Science Data*, *10*(3), 1503–1526. https://doi.org/10.5194/essd-10-1503-2018

Sánchez, L., Völksen, C., Sokolov, A., Arenz, H., & Seitz, F. (2018b). Present-day surface deformation of the Alpine Region inferred from geodetic techniques (data) Supplement to: Sánchez, L et al. (. *Present-day surface deformation of the Alpine region inferred from geodetic techniques. Earth System Science DataPANGAEA*, *10*(3), 1503–1526. https://doi.org/10.5194/essd-10-1503-2018

Serpelloni, E., Anzidei, M., Baldi, P., Casula, G., & Galvani, A. (2005). Crustal velocity and strain-rate fields in Italy and surrounding regions: New results from the analysis of permanent and non-permanent GPS networks. *Geophysical Journal International*, *161*(3), 861–880. https://doi.org/10.1111/j.1365-246X.2005.02618.x

Serpelloni, E., Faccenna, C., Spada, G., Dong, D., & Williams, S. D. P. (2013). Vertical GPS ground motion rates in the Euro-Mediterranean region: New evidence of velocity gradients at different spatial scales along the Nubia-Eurasia plate boundary. *Journal of Geophysical Research: Solid Earth*, *118*(11), 6003–6024. https://doi.org/10.1002/2013JB010102

Serpelloni, E., Vannucci, G., Anderlini, L., & Bennett, R. A. (2016). Kinematics, seismotectonics and seismic potential of the eastern sector of the European Alps from GPS and seismic deformation data. *Tectonophysics*, *688*, 157–181. https://doi.org/10.1016/j.tecto.2016.09.026

Shen, Z.-K., Jackson, D. D., & Kagan, Y. Y. (2007). Implications of geodetic strain rate for future earthquakes, with a five-year forecast of M5 earthquakes in southern California. *Seismological Research Letters*, *78*(1), 116–120. https://doi.org/10.1785/gssrl.78.1.116

Shen, Z.-K., Wang, M., Zeng, Y., & Wang, F. (2015). Optimal interpolation of spatially discretized geodetic data. *Bulletin of the Seismological Society of America*, *105*(4), 1–11. https://doi.org/10.1785/0120140247

Sillard, P., & Boucher, C. (2001). A review of algebraic constraints in terrestrial reference frame datum definition. *Journal of Geodesy*, *75*(2), 63–73. https://doi.org/10.1007/s001900100166

Smith, W., & Sandwell, H. (1997). Global sea floor topography from satellite Altimetry and ship depth soundings. *Science*, *277*(5334), 1956–1962. https://doi.org/10.1126/science.277.5334.1956

Sternai, P., Sue, C., Husson, L., Serpelloni, E., Becker, T. W., Willett, S. D., et al. (2019). Present-day uplift of the European Alps: Evaluating mechanisms and models of their relative contributions. *Earth-Science Reviews*, *190*, 589–604. https://doi.org/10.1016/j.earscirev.2019.01.005

Stucchi, M., Rovida, A., Gomez Capera, A. A., Alexandre, P., Camelbeeck, T., Demircioglu, M. B., et al. (2013). The SHARE European earthquake catalogue (SHEEC) 1000–1899. *Journal of Seismology*, *17*(2), 523–544. https://doi.org/10.1007/s10950-012-9335-2

Tarayoun, A., Mazzotti, S., Craymer, M., & Henton, J. (2018). Structural inheritance control on intraplate present-day deformation: GPS strain rate variations in the Saint Lawrence Valley, eastern Canada. *Journal of Geophysical Research: Solid Earth*, *123*(8), 7004–7020. https://doi.org/10.1029/2017JB015417

Vernant, P., Fadil, A., Mourabit, T., Ouazar, D., Koulali, A., Davila, J. M., et al. (2010). Geodetic constraints on active tectonics of the Western Mediterranean: Implications for the kinematics and dynamics of the Nubia-Eurasia plate boundary zone. *Journal of Geodynamics*, *49*(3), 123–129. https://doi.org/10.1016/j.jog.2009.10.007

Walpersdorf, A., Pinget, L., Vernant, P., Sue, C., Deprez, A., & team, t. R. (2018). Does long-term GPS in the Western Alps finally confirm earthquake mechanisms? *Tectonics*, *37*(10), 3721–3737. https://doi.org/10.1029/2018tc005054

Watson, G. A. (2006). Computing Helmert transformations. *Journal of Computational and Applied Mathematics*, *197*(2), 387–394. https://doi.org/10.1016/j.cam.2005.06.047

Webb, F. (1997). *Introduction to GIPsy/oasIs-II*. JPL D-11088.

Williams, S. D. P. (2003). The effect of coloured noise on the uncertainties of rates estimated from geodetic time series. *Journal of Geodesy*, *76*(9), 483–494. https://doi.org/10.1007/s00190-002-0283-4

Woessner, J., Laurentiu, D., Giardini, D., Crowley, H., Cotton, F., Grünthal, G., et al. (2015). The 2013 European seismic hazard model: Key components and results. *Bulletin of Earthquake Engineering*, *13*(12), 3553–3596. https://doi.org/10.1007/s10518-015-9795-1

Zumberge, J. F., Heflin, M. B., Jefferson, D. C., Watkins, M. M., & Webb, F. H. (1997). Precise point positioning for the efficient and robust analysis of GPS data from large networks. *Journal of Geophysical Research*, *102*(B3), 5005–5017. https://doi.org/10.1029/96jb03860

Zurutuza, J., Caporali, A., Bertocco, M., Ishchenko, M., Khoda, O., Steffen, H., et al. (2019). The Central European GNSS Research Network (CEGRN) dataset. *Data in Brief*, *27*, 104762. https://doi.org/10.1016/j.dib.2019.104762